# High Temperature DC SQUID Fabrication on Bicrystal YBCO Thin Films

by

Muhammet Ali Yurtalan

A thesis
presented to the University of Waterloo
in fulfillment of the
thesis requirement for the degree of
Master of Applied Science
in
Mechanical Engineering

Waterloo, Ontario, Canada, 2012

I hereby declare that I am the sole author of this thesis. This is a true copy of the thesis, including any required final revisions, as accepted by my examiners.

I understand that my thesis may be made electronically available to the public.

## Abstract

After the discovery of high temperature superconductors, different types of Josephson junctions were investigated and thus a new path is created to obtain high temperature superconducting quantum interface devices(SQUID). However fabrication of high temperature superconductors is a challenging concept. It is desired that the fabrication methods yield to high reproducibility and sensitive devices. Currently, SQUIDs are mostly realized by using bicrystal thin films and by making ramp edge junctions. In this study, nano scale fabrication of $Y_1Ba_2Cu_3O_7$ (YBCO) thin films on bicrystal $SrTiO_3$ (STO) substrates and implementing DC SQUIDs on these films are investigated.

YBCO thin films are deposited on STO substrates with RF magnetron sputtering using argon and oxygen gases. In order to obtain good quality films, deposited films are subjected to post annealing and followed by an oxidation process. After obtaining films, several characterization processes carried. Scanning electron microscopy (SEM) is used to analyze the surface and energy dispersive x-ray diffraction (EDX) is used to analyze the composition of the resulted thin films. Atomic force microscopy is also used to analyze the surface. Magnetic properties of the resulting films are then measured with SQUIDS integrated to magnetic property measurement systems (MPMS). AC susceptibility and voltage-current characterizations are done. Then the contact layer is deposited using DC sputtering system. A hard mask is then deposited to act as a mask during the etching process. In this case, $SiO_2$ is deposited using RF magnetron sputtering on Au thin layer. An e-beam resist coating is then followed. The resist is patterned by electron beam lithography to achieve 200nm resolution. The developed resist is then removed after the pattern transfer to $SiO_2$ by reactive ion etching (RIE). After the pattern is transferred via sputter etching of both YBCO and Au the final device is realized having Au on top of YBCO. The results for this experimental procedures are then summarized.

**Acknowledgements**

I would like to express my deep gratitudes to Prof. Mustafa Yavuz for supervising my studies and encouraging towards pursuing a graduate degree.

I am deeply indebted and would like to show my sincere gratitudes to my group friends who extensively helped me to carry out this thesis.

Finally I would really like to thank to my family who always supported and encouraged me during my studies in Waterloo

# Table of Contents

# List of Tables

# List of Figures

# Chapter 1

# Introduction

Superconducting quantum interface devices (SQUIDs) are currently the most sensitive magnetic flux detectors available. They can measure any physical quantity which can be related to magnetic field. Thus, SQUIDs have broad range of application areas such as biomagnetism and spin detection. General trend was to detect micro sized materials and smaller magnetic fields. There is an intense investigation of increasing the sensitivity of magnetic field detectors.

SQUIDs are generally composed of Josephson junctions on superconducting loops. Depending on the configuration, alternative SQUIDs have been realized. A DC SQUID is formed by interrupting a superconductor loop with two identical Josephson junctions connected in parallel. Josephson junctions are formed when two superconducting electrodes are separated by a thin non-superconducting layer. Classically, charge carrier in superconductors are confined to their local electrode in such case but quantum mechanically, these carriers can penetrate through the barrier. Thus, a tunneling current occurs, but the interesting phenomena is that this current does not dissipate energy, in other words, there is no voltage drop across the junction when certain conditions are met. If voltage drop occurs across the junction, this drop will respond to applied flux to the squid loop. Thus, a voltage-magnetic field relation is observed in these junctions. The interference of these

two junctions on a superconductor loop will result in a practical SQUID.

There have been many studies for the low temperature SQUIDs. The discovery of high temperature superconductors has driven many researchers to realize high temperature SQUIDs. Since high temperature superconductors are structurally different from low temperature superconductors, different junction types and fabrication methods are needed to be developed. This theses is devoted to fabricate YBCO thin films and DC SQUID on bicrystal films.

In the second chapter, the basics of the superconductivity are explained. Flux quantization and two characteristic lengths of superconductors, coherence length $\xi$ and penetration depth $\lambda$ are briefly introduced. Macroscopic theory and and limiting parameters for superconductors are also discussed. In the third chapter, the Josephson equations are derived and the tunneling phenomena is explained. Different junction types for high temperature superconductors are introduced. In Chapter 4, DC SQUIDs are discussed and favourite resistively shunted junction model is introduced. A brief insight to sensitivity and SQUID configurations is given. In Chapter 5, fabrication process for YBCO thin films and steps for patterning the SQUID are discussed. Deposition methods, etching patterning and characterization methods are investigated. Furthermore results are displayed in this chapter. Chapter 6 provides a brief summarized conclusion and future work of the thesis.

# Chapter 2

# Superconductivity

The electrical resistivity of many metals and alloys vanishes when cooled down below certain temperature, often near the temperatures that helium is liquid. This phenomenon is called superconductivity. After liquefying the helium in 1908, H. Kamerlingh Onnes was able to investigate the electrical properties of the pure mercury at lower temperatures. H.K. Onnes discovered that the resistance of mercury dropped to near zero at 4.2 K[1].

Several experiments were performed on mercury to justify this resistance drop and then on indium, tin and lead which show superconducting properties at 3.4K, 3.7K and 7.2K respectively. The disappearance of the resistance is well understood by the induced current in a superconducting ring sample. When the current is created on a superconducting loop, the current can flow without significant loss. It was shown that these currents or respective magnetic field have a lifetime of at least $10^5$ years. The temperature where the specimen goes into transition between normal phase and superconducting phase is called critical temperature, $T_c$. Above this temperature the superconductivity is suppressed and the sample is in normal state again. Later H.K. Onnes found out that, applied magnetic field can also suppress the superconducting state above critical value. This value is called critical magnetic field, $H_c$.

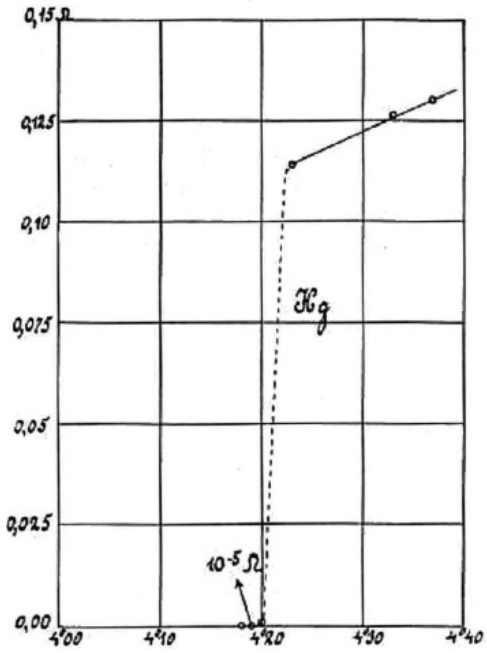


**Figure 2.1:** Resistance versus temperature of the Mercury[2].

## 2.1 Meissner Effect

In 1933 W. Meissner and R. Ochsenfeld discovered a relation between superconductivity and applied magnetic field. A superconducting element expelled the weak applied magnetic field form its interior below critical temperature $T_c$. On the other hand, in strong magnetic fields, superconductivity is ceased and the sample goes into transition to normal state again. This suggest that superconductors are not just ideal conductors. Consider the case where

| Element | $T_c$ in K | Compound | $T_c$ in K |
|---|---|---|---|
| Ti | 0.4 | NbTi | 10.0 |
| Al | 1.1 | $Nb_3Ge$ | 23.2 |
| Pb | 7.2 | $YBa_2Cu_3O_7$ | 90.0 |
| Nb | 9.5 | $Bi_2Sr_2Ca_2Cu_3O_{10}$ | 110.0 |

**Table 2.1:** Superconductivity of selected materials [2]

there are both ideal conductor and superconductor in their normal states, T>$T_c$. Then a magnetic field $B_a$ is applied. In normal state, the applied magnetic field penetrates both materials. When cooled below $T_c$, the applied field is expelled from superconductors unlike in the case where perfect conductors maintain its interior field. Figure 2.2 illustrates this phenomenon.

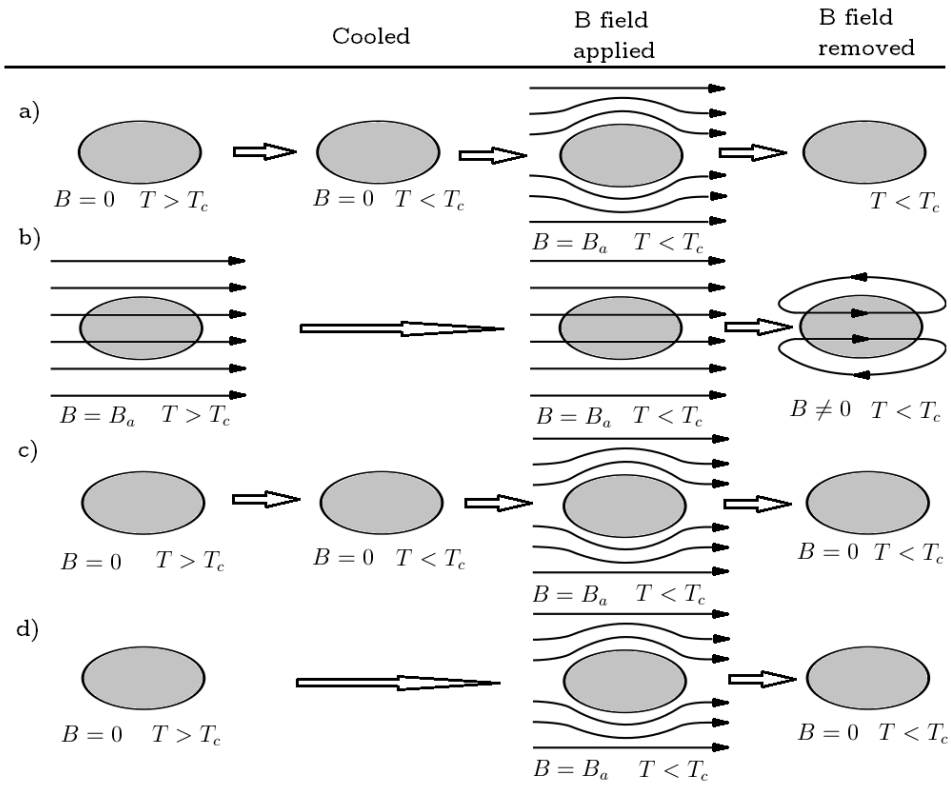


**Figure 2.2:** a)Ideal conductor: Magnetic field is applied after cool down. b) Ideal conductor: Magnetic field is applied before cool down. c) Superconductor: Magnetic field is applied after cool down. d) Superconductor: Magnetic field is applied before cool down.

Superconductors repel the magnetic field independent of the history of the applied magnetic field. Note that in order to expel this field, energy is needed which comes from the exothermic phase transition from normal to superconducting state of material. The expel of the field is done by the surface circulating currents which generate opposite field to

the applied magnetic field. So below $T_c$ and $H_c$ superconductor materials act as a perfect diamagnet.

## 2.2 London Theory

The first explanation of the Meissner-Ochsenfield was achieved by Heinz and Fritz London two years after the discovery, 1935. Their assumption was that the supercurrent is carried by a fraction of conduction electrons which experience no friction. The equation of motion of charged particle in an electric field is:

$$m_e \frac{\partial \vec{v}}{\partial t} = -e\vec{E} \tag{2.1}$$

This leads to an accelerated motion in the field. The super currentdensity is:

$$J_s = -en_s\vec{v} \tag{2.2}$$

Where $n_s$ is the super electron density. If followed up, The first London equation is obtained.

$$\frac{\partial \vec{J_s}}{\partial t} = \frac{n_s e^2}{m_e}\vec{E} \tag{2.3}$$

Remembering the Maxwell equation,

$$\vec{\nabla} \times \vec{E} = -\frac{\partial \vec{B}}{\partial t} \tag{2.4}$$

and taking the curl of 2.3, will lead to:

$$\frac{\partial}{\partial t}(\frac{m_e}{n_s e^2}\vec{\nabla} \times \vec{J_s} + \vec{B}) \tag{2.5}$$

This equation shows that the quantity in the parenthesis must be constant since the

time derivative is vanished. This equation well describes the behaviour of the ideal conductor but not the Meissner effect. To describe Meissner effect H. and F. London made another essential assumption that the quantity inside the parenthesis is not just an arbitrary constant but identical to zero. Then the second famous London equation is obtained.

$$\vec{\nabla} \times \vec{J}_s = -\frac{n_s e^2}{m_e} \vec{B} \tag{2.6}$$

Note that this assumption can not be justified with the classical physics. Current density in normal metals vanishes when no electric field is applied regardless there is a magnetic field penetrating the material or not. However, in type I superconductors, the equation 2.6 applies. Combining with the Maxwell equation,

$$\vec{\nabla} \times \vec{B} = \mu_0 \vec{J}_s \tag{2.7}$$

and equation 2.6 and with the help of the relation,

$$\vec{\nabla} \times (\vec{\nabla} \times \vec{B}) = -\nabla^2 \vec{B} \tag{2.8}$$

the equation for the magnetic field in a superconductor is obtained.

$$\nabla^2 \vec{B} - \frac{\mu_0 n_s e^2}{m_e} \vec{B} = 0 \tag{2.9}$$

In order to understand the equation 2.9 consider a simple sketch illustrated in figure 2.3. The applied magnetic field $B_0$ is parallel.

$$\frac{\mathrm{d}^2 B_y}{\mathrm{d}x^2} - \frac{1}{\lambda_L^2} B_y = 0 \tag{2.10}$$

while $\lambda_L$ is equal to:

$$\lambda_L = \sqrt{\frac{m_e}{\mu_0 n_s e^2}} \tag{2.11}$$

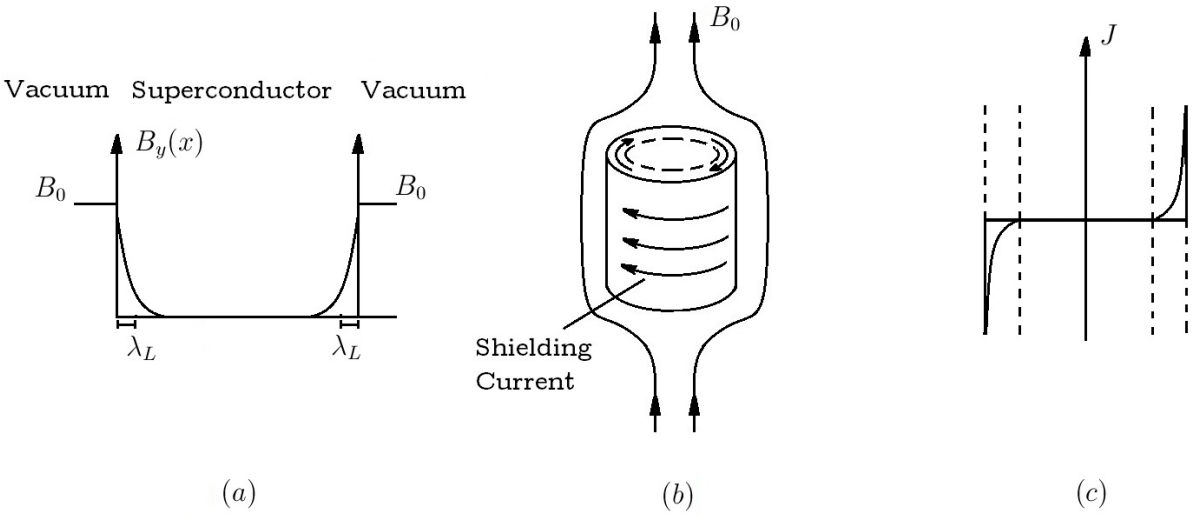


**Figure 2.3:** a)Magnetic field inside and outside of a superconductor. b) Representation of the expel of magnetic field and screening current. c) Screening current that creates opposing field.

The solution becomes:

$$B_y(x) = B_0 exp(-x/\lambda_L) \tag{2.12}$$

Here $\lambda_L$ is known as the London penetration depth. Instead stopping suddenly, the applied magnetic field penetrates to the superconductor from the surface to a certain distance, see figure 2.3. Typical superconductors have penetration depths of 20-50 nm. It can be concluded that the current is also bounded within this region defined by penetration depth since current inside creates magnetic field.

## 2.3 Thermodynamics of Superconductors

When the system is under the critical values of temperature and applied field, system goes into transition to superconducting state. Thermodynamically this state is more stable and

favorable. Lets consider a cylindrical sample in applied magnetic field $H < H_c$. Then $B = 0$, the meissner effect applies and magnetization is $M = -\mu_0 H$. If the applied field is increased by $dH$ then the work done by the field source is $MdH{=}{-}\mu_0 HdH$. If the field is increased from 0 to $H_0$ the total work of the source is

$$W = \mu_0 \int_0^{H_0} HdH = \frac{\mu_0 H_0^2}{2} \tag{2.13}$$

Free energy accumulated in the superconductor is equal to this work. Thus, if the applied field is $H_c$ then the free energy increase of the superconductor will be:

$$F_n(H_c) = F_s(0) + \frac{\mu_0 H_c^2}{2} \tag{2.14}$$

By definition the free energy is:

$$F = U - TS \tag{2.15}$$

Then

$$\partial F = \partial U - T\partial S - S\partial T \tag{2.16}$$

With the help of first law of thermodynamics:

$$\partial Q = \partial W - \partial U \tag{2.17}$$

Where $\partial Q$ is heat energy, $\partial W$ is work done by sample and $\partial U$ is internal energy change. For reversible process, like superconducting phase transition, $\partial Q = T\partial S$. Then:

$$\partial F = -\partial W - S\partial T \tag{2.18}$$

From equation 2.18 it can be concluded that the entropy is:

$$S = -\left(\frac{\partial F}{\partial T}\right)_W \tag{2.19}$$

If the entropies of the two states of the superconductivity is investigated,

$$S_s - S_n = -\frac{\partial}{\partial T}(F_s - F_n) \tag{2.20}$$

then it follows:

$$S_s - S_n = \mu_0 H_c \left(\frac{\partial H_c}{\partial T}\right) \tag{2.21}$$

Experiments showed that $\partial H_c/\partial T < 0$. This results $S_s - S_n < 0$. Here it is concluded that the superconducting state is more ordered than normal state since the respective entropy is smaller. The critical applied magnetic field, $H_c$, reaches a maximum value at $T \to T_0$ whereas 0 at $T = T_c$. It was observed that $H_c(T)$ obeys a parabolic equation[3]

$$H_c(T) \approx H_c(0)\left[1 - \left(\frac{T}{T_c}\right)^2\right] \tag{2.22}$$

Considering equation 2.22 it can be concluded that at $T = T_c$, $S_s = S_n$. Therefore, the transition occurs without heat, is second order phase transition.

## 2.4 Ginzburg-Landau Equations

Ginzburg-Landau theory is a phenomenological approach to superconductivity and it was build on the Landau‘s theory of second order phase transition. According to this theory, there is a physical quantity, order parameter, which defines the phases. For instance, the order parameter in ferromagnetism is magnetization. Above the critical transition temperature this order parameter value is vanished whereas under the critical temperature it is a non zero value. In the phase transition of superconductors the complex order parameter $\psi$ is used such that $|\psi|^2 = n_s$, where $n_s$ is the local concentration of the superconducting

electrons. In normal state, $|\psi|^2$ has a value of zero. In superconducting state this $|\psi|^2$ value has a finite value.

If the superconductor is put under an applied field and fixed temperature, in the equilibrium state its free energy is at minimum. The free energy for superconducting state can be constructed as the contribution from phase transition, kinetic energy, field energy and the free energy of the normal state.

In Landau's theory, the generic expression for the second order phase transitions is expressed as:

$$F_0(T) = \alpha|\psi|^2 + \frac{1}{2}\beta|\psi|^4 \tag{2.23}$$

The parameter $\alpha$ taken to be proportional to $T - T_c$ and $\beta$ to be a positive constant. while $T > T_c$, since the state is in normal state we have $|\psi|^2 = 0$. When $T < T_c$ we have $|\psi|^2$ to be a finite value and the free energy is at minimum when equilibrium is reached (see figure 2.4). If we take the derivative of equation 2.23 with respect to $|\psi|^2$ it is seen that:

$$|\psi|^2 = |\psi_\infty|^2 = \frac{\alpha}{\beta} \tag{2.24}$$

Since $\alpha$ is proportional to $T - T_c$ so does the $|\psi|^2$. However if we consider a large homogeneous specimen it will reach a constant value $|\psi_\infty|^2$ deep inside it in fixed temperature.

Second contribution is the kinetic energy of the super-electrons related to interaction with a field.

$$F_K = \frac{1}{2m^*}\left|\left(-i\hbar\nabla - e^*\vec{A}\right)\psi\right|^2 \tag{2.25}$$

Where $m^*$ is $2m_e$, mass of the superconducting electron pair and $e^*$ is $2e$, charge of the pair.

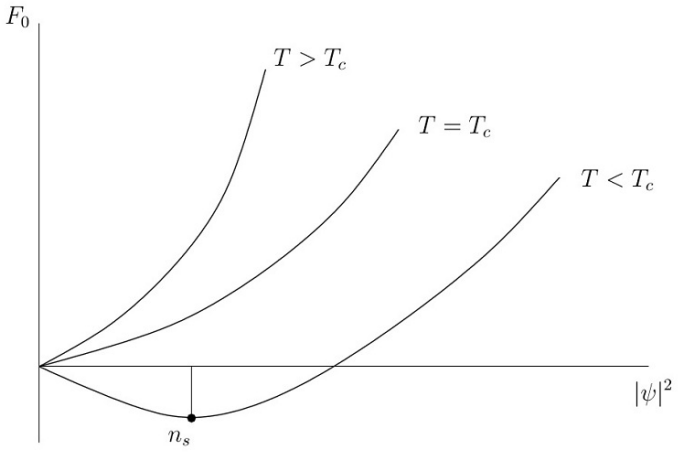


**Figure 2.4:** Free energy versus order parameter under different temperatures.

Third contribution is from the free energy of the magnetic field itself.

$$F_M = \frac{1}{2\mu_0} B^2 \tag{2.26}$$

Summing $F_0$, $F_K$ and $F_M$ will result in the expression for Ginzburg - Landau free energy.

$$F_{GL}(\vec{A}, \psi) = F_n + \int \alpha|\psi|^2 + \frac{1}{2}\beta|\psi|^4 + \frac{1}{2m^*}|(-i\hbar\nabla - e^*\vec{A})\psi|^2 + \frac{1}{2\mu_0}B^2 dV \tag{2.27}$$

Normally the field outside generated by external sources is fixed. Thus the Helmholtz free energy is used but inside the superconductor magnetic field is not fixed. So Gibbs free energy is considered for minimization.

$$G_s(\vec{A}, \psi) = F_n + \int \alpha|\psi|^2 + \frac{1}{2}\beta|\psi|^4 + \frac{1}{2m^*}|(-i\hbar\nabla - e^*\vec{A})\psi|^2 + \frac{1}{2\mu_0}B^2 - \vec{B}\vec{H} dV \tag{2.28}$$

Then famous GL equations are obtained by the minimization of the total free energy

function 2.28 with respect to variables $\psi$ and $\vec{A}$ respectively. If the variations $\delta G_s$ with respect to $\delta\psi$ is investigated the following equation is obtained[3].

$$\alpha\psi(r) + \beta|\psi(r)|^2\psi(r) + \frac{1}{2m^*}(-i\hbar\nabla - e^*\vec{A})^2\psi = 0 \tag{2.29}$$

Considering the intersection of the superconductor and normal states in a superconducting material the normalized wave function can be rewritten as $f = \psi/\psi_\infty$. The equation 2.29 becomes:

$$\frac{\hbar^2}{2m^*|\alpha|}\frac{d^2f}{dx^2} + f - f^3 = 0 \tag{2.30}$$

Then it is defined as the Ginzburg Landau Coherence length.

$$\xi^2(T) = \frac{\hbar^2}{2m^*|\alpha(T)|} \tag{2.31}$$

This coherence length can be interpreted as a distance where the order parameter changes, that is the distance between the normal and the superconducting states at the interface. The next Ginzburg Landau equation is obtained by investigating the variations of the $\delta G_s$ with respect to $\delta\vec{A}$[3].

$$\vec{J_s} = \nabla \times \left(\frac{1}{\mu_0}\nabla \times \vec{A}\right) = \frac{-i\hbar e^*}{2m^*}(\psi^*\nabla\psi - \psi\nabla\psi^*) - \frac{e^{*2}}{m^*}|\psi|^2\vec{A} \tag{2.32}$$

If the wave function is considered as $\Psi = |\Psi|e^{i\phi}$ then,

$$J_s = \frac{e^*}{m^*}|\psi|^2(\hbar\nabla\phi - e^*\vec{A}) \tag{2.33}$$

Remembering $J = 1/\mu_0(\vec{\nabla} \times \vec{B})$ and taking the curl, the equation 2.33 yields to:

$$\vec{\nabla} \times \left(\frac{1}{\mu_0}\vec{\nabla} \times \vec{B}\right) = -\frac{e^{*2}}{m^*}\vec{\nabla} \times \vec{A} \tag{2.34}$$

It is found:

$$\nabla^2 \vec{B} - \frac{1}{{\lambda_L}^2} \vec{B} = 0 \tag{2.35}$$

And ${\lambda_L}^2$ is:

$${\lambda_L}^2 = \frac{m^*}{e^* \mu_0 |\psi|^2} \tag{2.36}$$

The same result is obtained as the London penetration depth if $|\psi|^2 = n_s/2$. With the help of the Ginzburg Landau equations two characteristics lengths of superconductors, Coherence length $\xi$ and penetration depth $\lambda$ are obtained.

## 2.5 Flux Quantization

Another hallmark of the superconductors is that the magnetic field is quantized in a superconductor closed loop. Consider a hollow cylinder which has thick walls ($t > \lambda$) as in figure 2.5 which a magnetic flux is inside.

The wave function of the superconducting electron pair needs to be singe valued around any closed path.Thus there is a relation $\psi(0^+) = \psi(0^-)e^{2n\pi}$. This relation is obtained from:

$$\oint_C \vec{\nabla}\phi \cdot d\vec{l} = n2\pi \tag{2.37}$$

If the thickness of the wall is much more smaller than the penetration depth ($t << \lambda_L$) then the corresponding current is found to be zero for the contour C. Remembering the equation 2.33 and setting $J_s = 0$ yields to:

$$\nabla\phi = \frac{e^*}{\hbar} \vec{A} \tag{2.38}$$

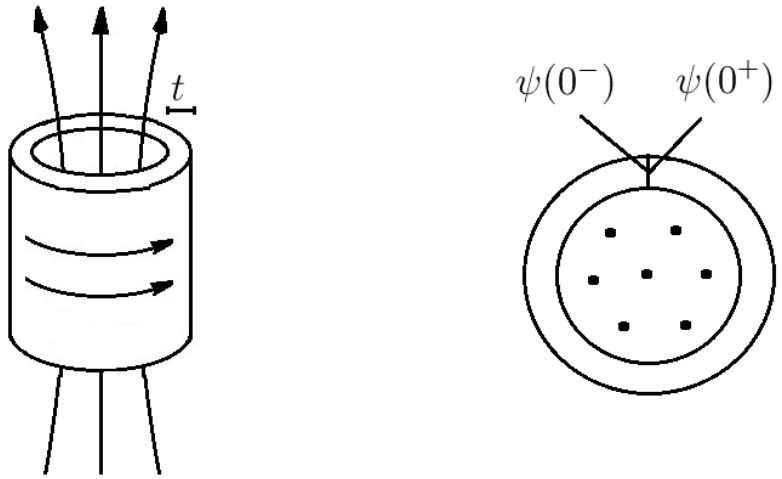


**Figure 2.5:** a) A cylinder with a magnetic field inside. b) Wave function of the SC electrons.

Hence,

$$\oint_C \vec{\nabla}\phi \cdot \vec{dl} = \frac{e^*}{\hbar} \oint \vec{A} \cdot \vec{dl} = n2\pi \tag{2.39}$$

$\oint \vec{A} \cdot \vec{dl} = \Phi$, it is followed that

$$\Phi = n\frac{h}{e^*} = n\Phi_0 \tag{2.40}$$

This means that, any magnetic field trapped in a hollow inside a superconductor will be integer multiplication of the magnetic flux quantum $\Phi_0 = \frac{h}{e^*}$.

## 2.6 Types of Superconductors

Superconductors can be categorized into two groups, type I and type II superconductors, when their respective response to applied field and current characteristics are concerned.

Most of the pure elemental superconductors are of type I whereas superconducting alloys and ceramics are of type II superconductors. In previous sections it is expressed that superconductors will expel the applied field applied on it. This is the exact case for type I superconductors. However type II superconductors have two critical values for the applied magnetic field. Below $H_{c1}$ the meissner effect is fully applied. If the applied field is between these two critical values $H_{c1} < H_a < H_{c2}$ then the system is in mixed state, that is, the applied field can penetrate through the sample in certain amounts leading a cylindrical normal phase regions in superconductor domain.The specimen remains electronically superconductor. Type II superconductors are used often in application since they have higher critical field values ($H_{c2} >> H_c$) and remain superconductor in relatively high temperatures. Typical critical field values for type I superconductors are around 0.01-0.1$T$ for magnetic field and $< 9K$ for temperature. For YBCO, which is a type II superconductor, $H_{c2} > 100T$ and $T_c$ is around $92K$[4]

Another important fact that distinguishes type I and type II superconductors is that relation between the coherence length and the penetration depth. If the coherence length $\xi$ is longer than the penetration depth $\lambda$ then the specimen is defined as type I. But if the coherence length is shorter, then the superconductor is type II. Figure 2.7 illustrates this. The parameter $\kappa$, known as Ginzburg landau parameter, is used to define types of superconductors as $\kappa = \lambda/\xi$. For type II, $\kappa < 1/\sqrt{2}$. It is noted that when the $\lambda >> \xi$, the surface energy between superconductor and normal region interface is negative. Thus magnetic field can penetrates into the specimen as quantized vortices, each having a magnetic flux $\Phi = h/e^*$[5].

## 2.7 Vortices

In 1957, A.A. Abrikosov calculated that the energy at the interface is negative in some superconductors. That is, there is a new state which has lower energy than the meissner state. Abrikosov predicted that there is an arranged lattice of magnetic field penetrations

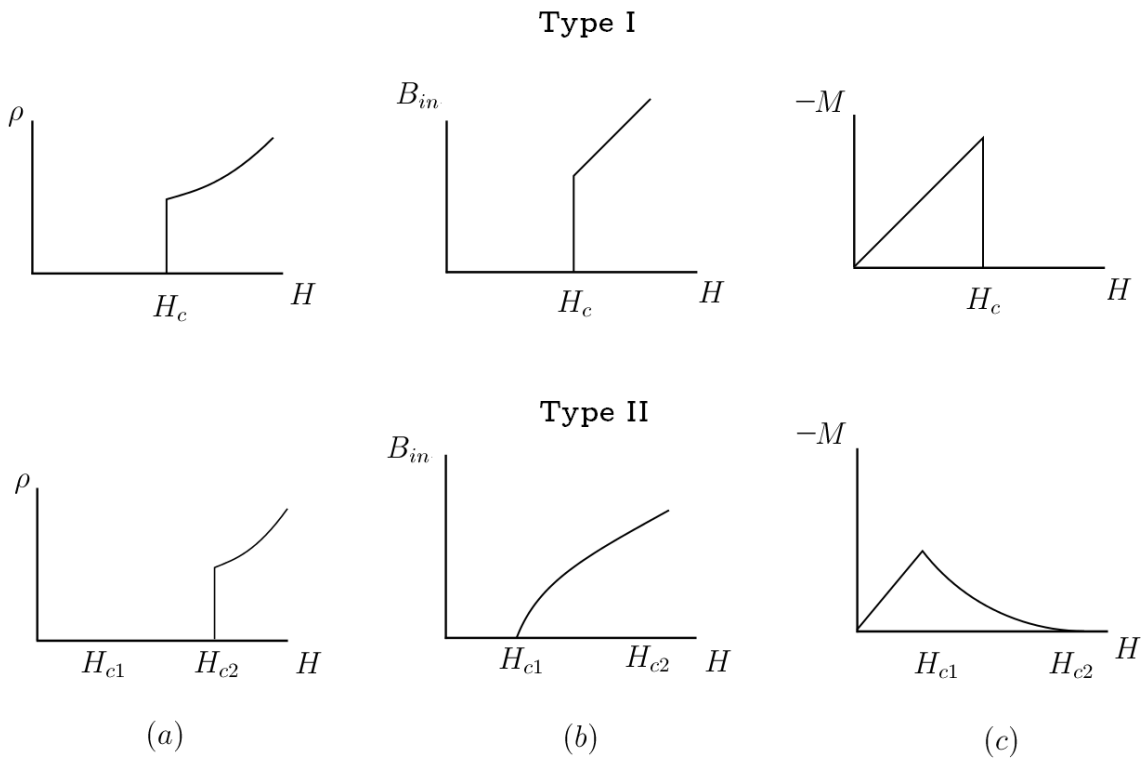


**Figure 2.6:** Comparison of Type I and Type II superconductors. a) Resistivity versus applied magnetic field. b) Magnetic field inside superconductor versus applied magnetic field. c) Magnetization versus applied field.

into specimen. First, he stated that these quantized vortices form a square lattice which had the smaller energy[6]. But later he found that triangular lattice is more favorable.A single vortex has a nucleus of normal state having a size about $2\xi$. Since the field penetrates there exist a circulating current around this vortex core. Remembering the penetration depth one can comment that the region where this shielding current flows is about $2\lambda$, see figure 2.8.

Since vortices have magnetic field and shielding current around, it can be concluded that vortices interact with each other in an electromagnetic way. There will be a repulsive force

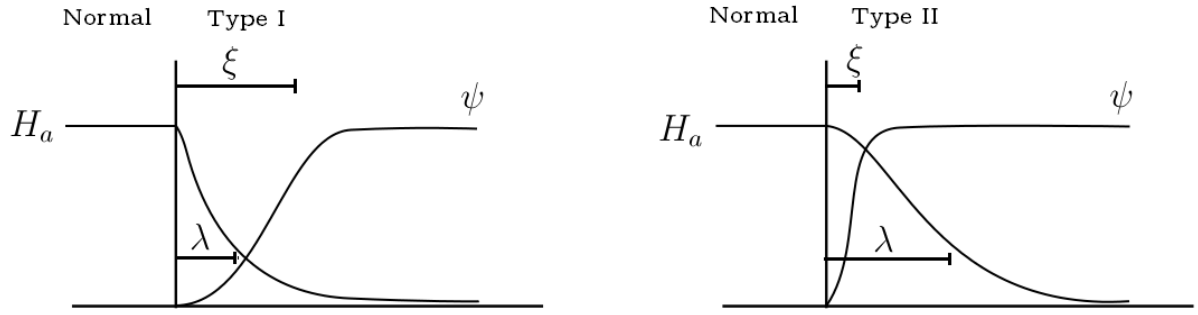


**Figure 2.7:** Coherence length and penetration depth representation of a) Type I b) Type II superconductors.

which tends to force these vortices form a lattice. Also, if the superconductor is driven by a current, vortices will feel a Lorentz force and start to creep . However, this movement will dissipate power and cease the superconductivity[7]. To overcome this problem, pinning mechanism of vortices via impurities are realized. If the pinning potential is enough, a high current can be driven by the superconductors which is an advantage of the type II superconductors over type I.

## 2.8 BCS Theory

In 1957, J. Bardeen, L.N. Cooper, J.R. Schrieffer constructed a theory which explains the superconductivity in microscopic point of view. The key element in BCS theory is that there exists an electron pair which are close to the Fermi level and pairing electrons are in interaction with the crystal lattice. It was found out that this interaction with the lattice allow two electron to be pairs and attracted to each other which overcomes the Coulomb repulsion force. The source of the lattice-electron energy is sustained by phonons. More specifically an electron moving through a cation lattice will distort the lattice around it resulting an increased local potential. Another electron with opposite spin at some distance is attracted by this ion distortion(self created phonon). Thus, this creates an indirect coupling of electrons, which are know to be cooper pairs having a distance of $\sim \xi$.

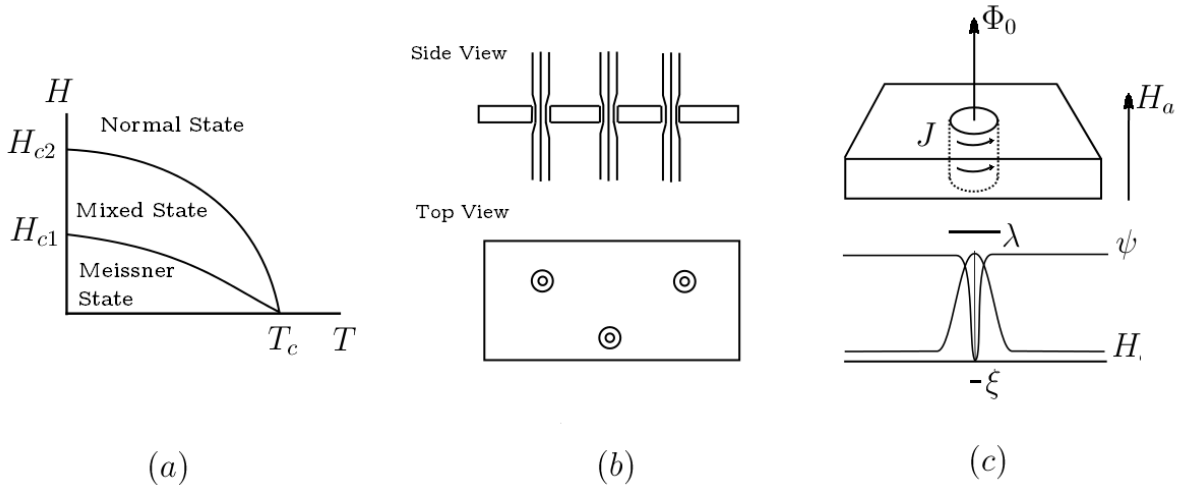


**Figure 2.8:** a) Sketch of temperature dependence of critical fields and respective states. b) Representation of the vortices and vortex lattice in a sample. c) Sketch of a single quantized ($\Phi_0$) vortex having a shielding current $J$ around its normal conducting core ( $2\xi$). It has a magnetic field distribution over $2\lambda$.

Cooper pairs have a charge of $2e$ and mass of $2m_e$ and the total spin is zero hence they can be considered as bosons which condense in to same energy level. With this mechanism, cooper pair movement will not feel any resistance in superconducting medium[8].

The essential point is that there is an energy gap between cooper electron state and normal single electron states in energy spectrum at Fermi level. Cooper pairs have slightly lower energy than the normal state electrons in the order of $\sim 10^{-4}E_F$[2] which is around $0.001ev$. Thus, thermal energies lower than the band gap energies of superconductors will lead to a zero resistivity. This can be considered as temperatures below $T_c$ have lower thermal energies compared to band gap energy.

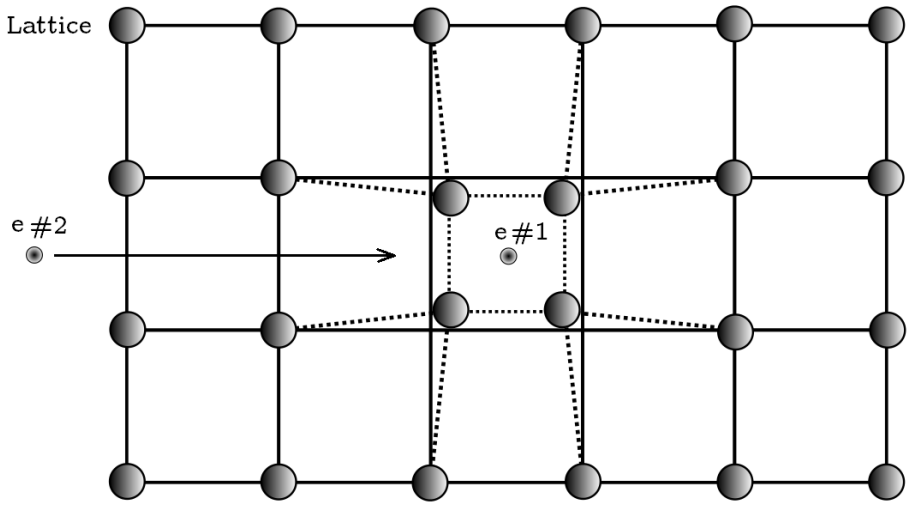


**Figure 2.9:** Schematic representation of electron-phonon-electron interaction. Electron 1 creates a distortion in lattice and electron 2 is attracted to this region.

## 2.9 Critical Current Density

Besides the applied magnetic field and temperature, there is another factor that affects the superconductivity which is the driven current density. Superconductors can support and still remain superconductor up to a critical value of current density. It can be related with the density of the electrons and their respective velocity. Cooper pairs will decouple if their respective energy exceeds the binding energy and the material will show normal state conductivity[9].

Figure 2.10 represent a critical surface phase diagram of $T_c$, $H_c$ and $J_c$ below which the specimen is in the superconducting state. Here it can be seen the relations of critical values between each other.

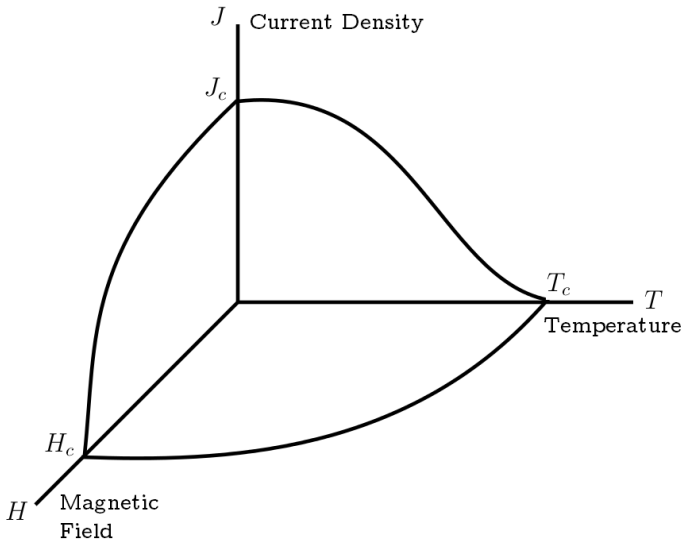


**Figure 2.10:** Sketch of critical values for magnetic field, temperature and current density and the surface represents the superconducting state.

# Chapter 3

# Josephson Junctions

## 3.1 Introduction

The idea of Josephson Junctions relies on the tunneling phenomena of the cooper pairs in two superconductor electrodes separated by a barrier such as insulating layer. Since cooper pairs show bosonic particle attributes they can all be in the same energy level. If the temperature is near $0K$, the majority of these cooper pairs will be in the same state known as the ground state. Thus the wave function is considered to be common to all cooper pairs in superconductor. Cooper pairs facing a barrier one expect the wave function of the cooper pairs to be decayed in the barrier layer and the corresponding supercurrent to be vanished. In 1962, B.D. Josephson predicted the tunneling phenomenon of the cooper pairs in superconductor electrodes separated by a resistive layer.

If the width of this layer is smaller than the coherence length $\xi$ of the superconducting material and the current is below its critical value, cooper pairs can tunnel through the barrier. Corresponding supercurrent can penetrate through barrier without any voltage drop. This Josephson effect is behind many superconducting quantum devices such as SQUIDs ( superconducting quantum interference devices ).

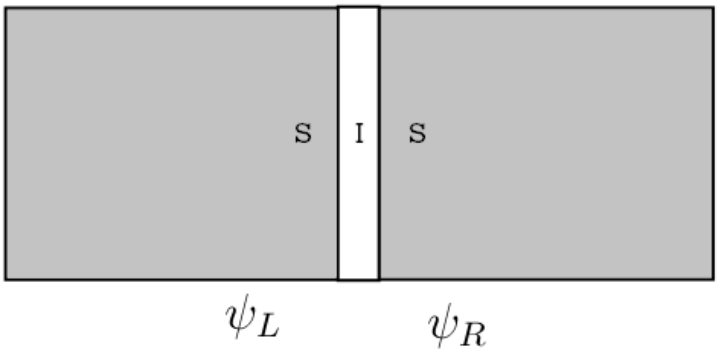


**Figure 3.1:** A superconductor-insulator-superconductor (SIS) trilayer.

## 3.2 Josephson Equations

Consider a superconductor-insulator-superconductor type junction represented in figure 3.1. Let the order parameter $\psi_L$ to represent the wave function of coopers pairs of the left superconductor and $\psi_R$ of the right superconductor. $|\psi_L|^2 = n_L$ represents the cooper pair density $n_L$ in the left superconductor and $|\psi_R|^2 = n_R$ in right superconductor. There exist a weak coupling of the superconductors, thus transfer of the cooper pairs between states $L$ and $R$ is possible. Thus additional terms for the respective wave functions are built with a constant factor which is determined by the characteristics of the junction. This K term allows wave functions to tunnel through one into other superconductor. The Schrodinger's equation for superconductors are:

$$\begin{aligned} i\hbar\frac{\partial\psi_L}{\partial t} &= \hat{H}\psi_L + K\psi_R \\ i\hbar\frac{\partial\psi_R}{\partial t} &= \hat{H}\psi_R + K\psi_L \end{aligned} \tag{3.1}$$

Where $\hat{H}$ is the Hamiltonian energy operator. Here it is assumed that the eigen value for hamiltonian operator is the energy state for each superconductor $\hat{H}\psi_{L,R} = E_{L,R}\psi_{L,R}$, then

the equations 3.1 becomes:

$$\begin{aligned} i\hbar\frac{\partial\psi_L}{\partial t} &= E_L\psi_L + K\psi_R \\ i\hbar\frac{\partial\psi_R}{\partial t} &= E_R\psi_R + K\psi_L \end{aligned} \tag{3.2}$$

If the superconductors are identical then the energies of the superconductors will be same which could be cancelled. If there is a potential difference V across the junction, there will be an energy difference in ground state energies $E_L - E_R = e^*V = 2eV$. If we define a zero energy in halfway between the junction equations 3.2 can be rewritten as:

$$\begin{aligned} i\hbar\frac{\partial\psi_L}{\partial t} &= (+eV)\psi_L + K\psi_R \\ i\hbar\frac{\partial\psi_R}{\partial t} &= (-eV)\psi_R + K\psi_L \end{aligned} \tag{3.3}$$

These equations are the standard equations that describes the two quantum mechanically coupled states[10]. Remembering and taking the derivative with respect to time of $\psi_{L,R} = \sqrt{n_{L,R}}e^{i\phi_{L,R}}$ will give:

$$\dot{\psi}_{L,R} = \frac{1}{2\sqrt{n_{L,R}}}\dot{n}_{L,R}\; e^{i\phi_{L,R}} + i\sqrt{n_{L,R}}\;\dot{\phi}_{L,R}\; e^{i\phi_{L,R}} \tag{3.4}$$

If we put the equation 3.4 in to equations 3.3 and rearrange, it will yield to:

$$\begin{aligned} \frac{\dot{n_L}}{2\sqrt{n_L}} + i\sqrt{n_L}\dot{\phi_L} &= \frac{-i}{\hbar}(+eV)\sqrt{n_L} - \frac{-i}{\hbar}K\sqrt{n_R}\; e^{(\phi_R-\phi_L)} \\ \frac{\dot{n_R}}{2\sqrt{n_R}} + i\sqrt{n_R}\dot{\phi_R} &= \frac{-i}{\hbar}(-eV)\sqrt{n_R} - \frac{-i}{\hbar}K\sqrt{n_L}\; e^{(\phi_L-\phi_R)} \end{aligned} \tag{3.5}$$

Where $\phi_{L,R}$ is the macroscopic phase of the superconductors. If the real parts are equated then the following equation is obtained:

$$\dot{n_L} = \frac{2}{\hbar} K \sqrt{n_L n_R}\ \sin(\phi_R - \phi_L) \tag{3.6}$$

$$\dot{n_R} = \frac{-2}{\hbar} K \sqrt{n_L n_R}\ \sin(\phi_R - \phi_L) \tag{3.7}$$

The equations for the imaginary parts will be:

$$\dot{\phi_L} = -\frac{K}{\hbar}\sqrt{n_R/n_L}\cos\phi_R - \phi_L - \frac{eV}{\hbar} \tag{3.8}$$

$$\dot{\phi_R} = -\frac{K}{\hbar}\sqrt{n_R/n_L}\cos\phi_R - \phi_L + \frac{eV}{\hbar} \tag{3.9}$$

Here it can be concluded that the time derivative of the charge densities represents the tunneling current across the junction. It can be interpreted form equation 3.7.

$$J = \tfrac{2}{\hbar} K \sqrt{n_L n_R}\ \sin(\phi_R - \phi_L)$$

$$J = J_0 \sin\phi \tag{3.10}$$

Where $\phi = \phi_R - \phi_L$. Since $n_R$ and $n_L$ are constants and equal to $n_0$, then $J_0 = 2Kn_0/\hbar$ and $J_0$ is a constant characteristic of the junction. If we are to investigate the phase difference $\phi$ with the help of equation 3.9 it follows as:

$$\frac{\partial\phi}{\partial t} = \frac{2eV}{\hbar} \tag{3.11}$$

Equations 3.10 and 3.11 are the famous Josephson relations.

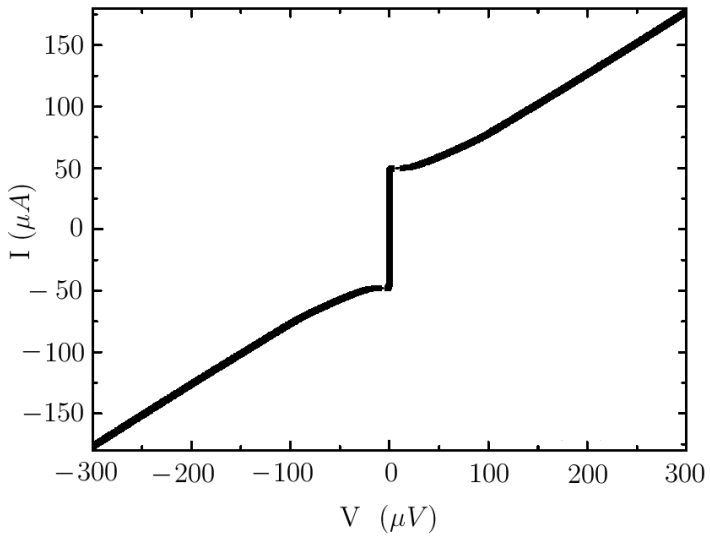


**Figure 3.2:** Graphical representation of current voltage characteristics of YBCO SQUID showing the current at zero voltage[11].

## 3.3 DC Josephson Effect

If the voltage across the junction equals to zero, the relation 3.11 implies that the time derivative of the phase difference is zero, meaning a constant $\phi$ but not necessarily to be zero and equation 3.11 predicts that a finite dissipationless DC current density $J_0$ can flow through the barrier without any voltage applied to the junction. This is the DC Josephson effect. The current density from $J_0$ to $-J_0$ is determined by the phase difference $\phi$.

## 3.4 AC Josephson Effect

When a DC voltage V is applied (or a DC current density larger than $J_0$ ) an oscillating supercurrent is generated. If the equation 3.11 is integrated with respect to time following is obtained.

$$\phi = \phi_c + \frac{2e}{\hbar} Vt \tag{3.12}$$

Leading to a current density which has argument in the sine function.

$$J = J_0 \sin\left(\phi_c + \frac{2e}{\hbar} V t\right) \tag{3.13}$$

This oscillation in the current gives rise to an electromagnetic radiation with a frequency of $v = (2e/h)V$, known as Josephson frequency where $2e/h$ has a value of 483.6 GHz/mV.

## 3.5 Josephson Tunneling

The Josephson equations are derived considering a SIS junction type. The dynamics of the tunneling mechanism in the insulating layer will be discussed in this subsection. Consider a junction shown in figure 3.3 which has a insulating barrier of thickness $d$ and have a potential energy of $V_0$. Time dependent macroscopic wave function can be rewritten as:

$$\psi(\mathbf{r}, t) = \psi(\mathbf{r}) e^{-i(E_0/\hbar)t} \tag{3.14}$$

In order to have a tunneling phenomena, The barrier energy $V_0$ must be bigger than the respective energy of this particular wave function of electrons. Classically the current can not penetrate through this barrier, however this tunneling behaviour is well explained quantum mechanically. Lets assume $\psi$ is the wave function of cooper electrons is insulating layer having an energy $E_0$.

If we assume the barrier potential is uniform and cooper pair current density is uniform that the problem reduces to one dimensional tunneling problem. Here $\psi$ in the region $-\frac{d}{2} < x < \frac{d}{2}$ can be expressed as:

$$\psi = C_1 \cosh(\kappa x) + C_2 \sinh(\kappa x) \tag{3.15}$$

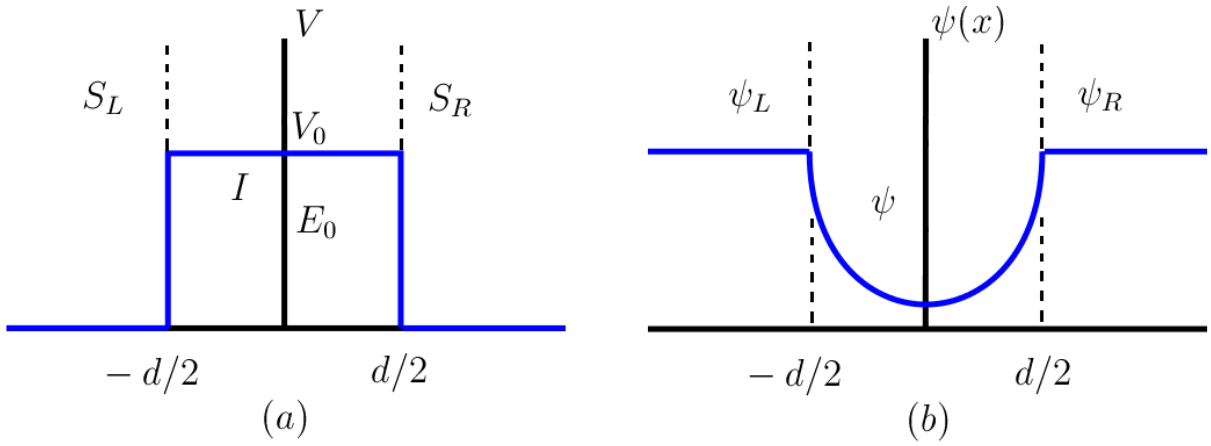


**Figure 3.3:** A SIS junction a) Energy of the barrier. b) Wave function representation of cooper pairs in 3 regions.

where the effects of the characteristics of barrier is implemented in constant $\kappa$.

$$\kappa = \sqrt{\frac{2m^*(V_0 - E_0)}{\hbar^2}} \tag{3.16}$$

If we are to look at the behaviour of $\psi$ at boundaries it is seen that:

$$\psi(-\frac{d}{2}) = \sqrt{n_L}e^{i\phi_L} \tag{3.17}$$

$$\psi(\frac{d}{2}) = \sqrt{n_R}e^{i\phi_R} \tag{3.18}$$

These equations will lead to:

$$\sqrt{n_L}e^{i\phi_L} = C_1\cosh(\kappa d/2) - C_2\sinh(\kappa d/2) \tag{3.19}$$

$$\sqrt{n_R}e^{i\phi_R} = C_1\cosh(\kappa d/2) + C_2\sinh(\kappa d/2) \tag{3.20}$$

Therefore solving for $C_1$ and $C_2$ followings are obtained.

$$C_1 = \frac{\sqrt{n_L}e^{i\phi_L} + \sqrt{n_R}e^{i\phi_R}}{2\cosh(\kappa d/2)} \tag{3.21}$$

$$C_1 = -\frac{\sqrt{n_L}e^{i\phi_L} - \sqrt{n_R}e^{i\phi_R}}{2\cosh(\kappa d/2)} \tag{3.22}$$

In the absence of any magnetic field the supercurrent density 2.32 can be written as:

$$\begin{aligned} \vec{J_s} &= \frac{-i\hbar e^*}{2m^*}(\psi^*\nabla\psi - \psi\nabla\psi^*) \\ &= \frac{e^*}{m^*}\Re\left\{\psi^*(-i\hbar\nabla)\psi\right\} \end{aligned} \tag{3.23}$$

Substituting the wave function $\psi$ the supercurrent density is expressed as:

$$\vec{J_s} = \frac{e^*}{m^*}\kappa\hbar\ \Im\{A^*B\} \tag{3.24}$$

With the help of equations 3.22 and using trigonometric identity, the supercurrent density is rewritten as:

$$J_s = J_0\sin(\phi_R - \phi_L) \tag{3.25}$$

Where the maximum critical current density is found to be as:

$$\vec{J_0} = -\frac{e^*}{m^*}\kappa\hbar\frac{\sqrt{n_L n_R}}{2\sinh(\kappa d/2)\cosh(\kappa d/2)} = -\frac{e^*\kappa\hbar}{m^*}\frac{\sqrt{n_L n_R}}{\sinh(2\kappa d)} \tag{3.26}$$

The barrier height $V_0$ is typically around few $eV$ and the decay length $1/\kappa$ is less than a nanometer.

## 3.6 Junctions in Magnetic Field

In order to calculate the effect of magnetic field on Josephson tunneling current, a junction in figure 3.4 is considered. Two superconducting electrodes are separated by a thin barrier layer having a thickness of $d$. The junction have dimensions of L and W in $x$-$y$ plane and the current flows in $z$ direction. The magnetic field is parallel to $y$-axis. The field penetrates into the superconductors up to the penetration depth thickness $\lambda$, so the effective barrier thickness could be considered as $d + \lambda_L + \lambda_R$. In order to discuss the effect lets consider a contour shown in figure 3.4. It is demanded that the total phase change along this closed contour is needed to be an integer multiplication of $2\pi$, $\vec{\nabla}\phi \cdot \vec{dl} = 2\pi n$.

$$\vec{\nabla}\phi \cdot \vec{dl} = (\phi_{Q_R} - \phi_{Q_L}) + (\phi_{P_R} - \phi_{Q_R}) + (\phi_{P_L} - \phi_{P_R}) + (\phi_{Q_L} - \phi_{P_L}) + 2\pi n \tag{3.27}$$

Remembering the equation 2.33 and rewriting it for $\nabla\phi$ following is obtained.

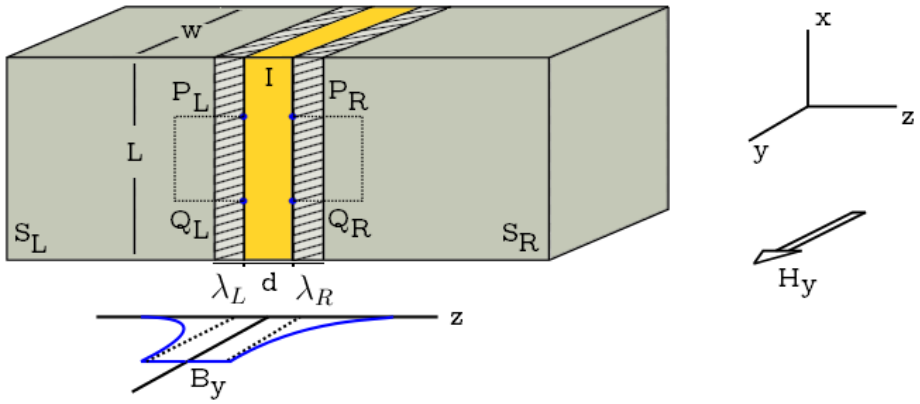


**Figure 3.4:** Contours of integration used to calculate the effects of magnetic field to Josephson current. Striped zone indicates the region where the magnetic field penetrates.

$$\nabla\phi = \frac{e^*}{\hbar}\left(\frac{m^*}{e^{*2}n}\vec{J}_s + \vec{A}\right) \tag{3.28}$$

Lets calculate the phase difference between point Q ($x$) and P ($x + \Delta x$) by integrating along the paths it is obtained:

$$\phi_{Q_R} - \phi_{P_R} = \frac{e^*}{\hbar} \int_{C_R} \left( \frac{m^*}{e^* n} \vec{J}_s + \vec{A} \right) \cdot \vec{dl}$$
$$\phi_{P_L} - \phi_{Q_L} = \frac{e^*}{\hbar} \int_{C_L} \left( \frac{m^*}{e^* n} \vec{J}_s + \vec{A} \right) \cdot \vec{dl} \tag{3.29}$$

Here it can be concluded that part of the contours are perpendicular to $J_s$ the first terms in the integrals can be neglected. If the thicknesses of the superconductors are larger than the penetration depths, contours can be expanded where the $J_s$ vanishes.

$$\phi(x + \Delta x) - \phi(x) = [\phi_{Q_L} - \phi_{Q_R}] - [\phi_{P_L} - \phi_{P_R}]$$

$$\phi(x + \Delta x) - \phi(x) = \frac{e^*}{\hbar} \left[ \int_{C_L} \vec{A} \cdot \vec{dl} + \int_{C_R} \vec{A} \cdot \vec{dl} \right] \tag{3.30}$$

Furthermore if we neglect the barrier thickness equation 3.30 becomes:

$$\phi(x + \Delta x) - \phi(x) = \frac{e^*}{\hbar} \oint \vec{A} \cdot \vec{dl} \tag{3.31}$$

The line integral can be replaced with surface integral of applied field since $\nabla \times \vec{A} = \vec{H}$:

$$\oint \vec{A} \cdot \vec{dl} = H_y(\lambda_L + \lambda_R + d)dx \tag{3.32}$$

Putting equation 3.32 into equation 3.31 it becomes:

$$\frac{d\phi}{dx} = \frac{e^*}{\hbar} H_y(\lambda_L + \lambda_R + d) \tag{3.33}$$

Lets define $t$ as effective barrier thickness $(\lambda_L + \lambda_R + d)$. The integration will lead to:

$$\phi = \frac{e^*}{\hbar} t H_y x + \phi_0 \tag{3.34}$$

Equation 3.34 suggests that the phase is spatially modulated by the applied magnetic field. Here the Josephson relation 3.10 can be rewritten as:

$$J = J_0 \sin(\frac{e^*}{\hbar} t H_y x + \phi_0) \tag{3.35}$$

Due to modulation on phase the current density is also modulated but is has periodicity. The analytic expression can be written as:

$$J_m(H) = J_0(0) \left| \frac{\sin \pi \frac{\Phi}{\Phi_0}}{\pi \frac{\Phi}{\Phi_0}} \right| \tag{3.36}$$

This relation summarizes the effect of the magnetic field on the junction critical current density. Figure 3.5 illustrates this phenomenon.

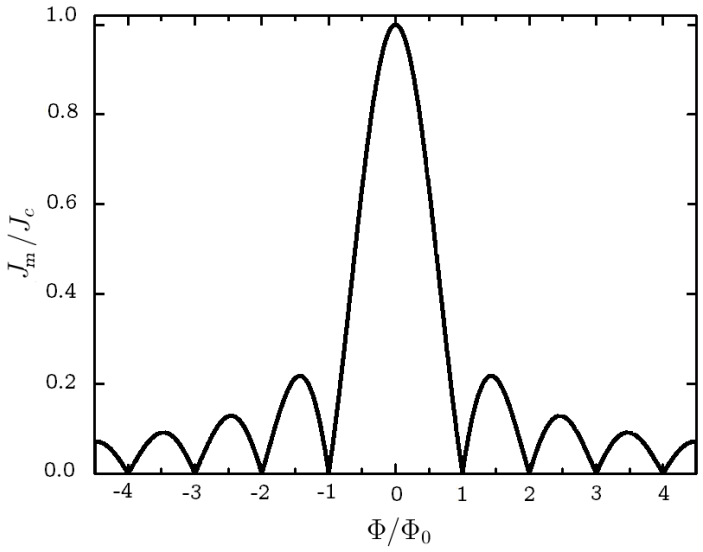


**Figure 3.5:** Magnetic field dependence of maximum critical current.

The behaviour of critical current under the magnetic field is analogous to the diffraction of light by a single slit. The minimum of the current is observed at integer multiplies of flux quantum $\Phi_0$. If there is a two Josephson junctions connected parallel by superconducting

region the quantum interference is observed[12]. The total supercurrent due to interference is given as:

$$I = 2I_0 \left| \cos \pi \frac{\Phi}{\Phi_0} \right| \tag{3.37}$$

Which is to be explained in following chapter.

## 3.7 High-Temperature Josephson Junctions

High temperature superconductors have an anisotropy between different directions when the supercurrent is considered. Thus they are analogously different compared to low temperature superconductors. Due to the this property many other Josephson junction types were investigated[13]. Here, these junction types are roughly categorized in three groups as *weakened junctions*, *extrinsic junctions* and *intrinsic junctions* which are to be explained.

### 3.7.1 Weakened Junctions

The idea of this type of weak links is that the superconductivity is distorted locally to act as a barrier. The resulting layer will have different properties than the superconducting electrodes. The size of this weakened barrier is important since it is demanded that the barrier is in the order of coherence length. The weakening of the superconductor region is mainly done by depositing superconducting films on thin stripes, by illumination of highly energetic ions and by controlled electrical pulses applied at micro bridges which distort the superconductivity in the bridge. It is reported that the aluminum stripes can locally distort the superconductivity of micro-bridges by reducing its transition temperature[14]. For the other method, a hard mask is patterned with the help of electron beam lithography since smaller dimensions are needed. The hard mask is used for ion illumination to define an exposed area having smaller transition temperature compared to superconductor islands.

This type of weak links might proven to be useful if the micro-bridge size can be lowered in to the order of coherence length. However, long term stability, reproducibility with same

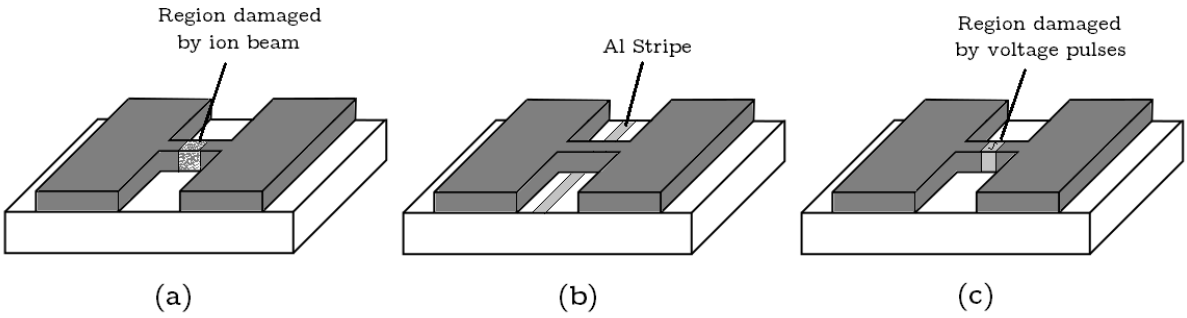


**Figure 3.6:** a) Weak link created by ion illumination. b) Weak links formed by depositing films on Al stripes. c) Weak links formed by electrical pulses on micro-bridges.

characteristics and narrow critical current tolerances need to be more investigated in locally damaged materials.[15]

### 3.7.2 Extrinsic Junctions

Josephson junctions including external material as barrier are considered as extrinsic junctions. Superconductor electrodes have a barrier in between them which is generally a normal (S-N-S) or a insulator material (S-I-S). The Josephson equations are derived with respect to superconductor-insulator-superconductor (S-I-S) types of weak links. In order to define the junction behaviour, it is crucial to have good control over these external materials. Here, instead of classic sandwich junctions, *SNS step edge junctions* and *ramp edge junctions* are described. The junctions in SNS-step edge junctions are formed by creating a steep step between non-contacting superconducting electrodes and a normal metal layer between these to regions to act as a barrier. Figure 3.7 illustrates the fabrication steps for SNS-step edge type junctions.

To have steep steps, (1) substrate is first coated with resist and patterned. after that the substrate is subjected to ion milling to create the step. (2) The resist is removed by

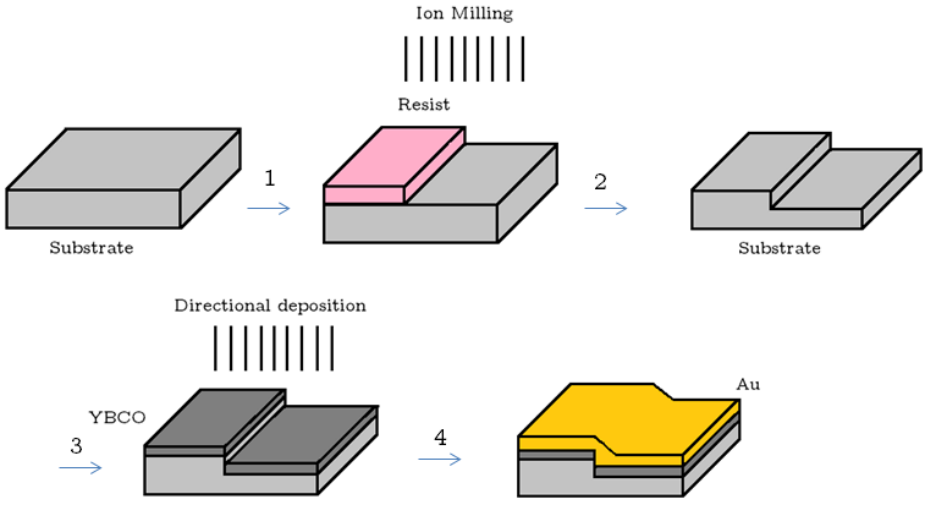


**Figure 3.7:** Fabrication process of SNS-step edge weak links.

proper solutions after exposure. (3) Directional deposition of the desired superconductor is then followed. Here it is important that there is a gap between superconductor electrodes. The reason is that, there may occur a grain boundar type junction if they are in contact. (4) After electrode deposition, the metal barrier is deposited in between superconductors. This metal layer is generllay chosen to act as a contact as well then contacts are formed if desired.

There are successful junctions reported having a critical current density of $10^5 A/cm^2$[16]. The potential advantages of this junction type is that it has low capacitance, a possibility of uniform superconductor-normal interfaces, low noise and relatively easy fabrication steps. However using same parameters, obtaining the same junction behaviors while reproduction is low. There exist some fluctuations in critical current[17].

Another method for creating an extrinsic junction is to use insulator layers as barriers. One of the most studied junction is ramp edge junctions. The fabrication process for ramp edge junctions are showed in figure 3.8. Generally ramp edge junctions have a barrier of insulating material.

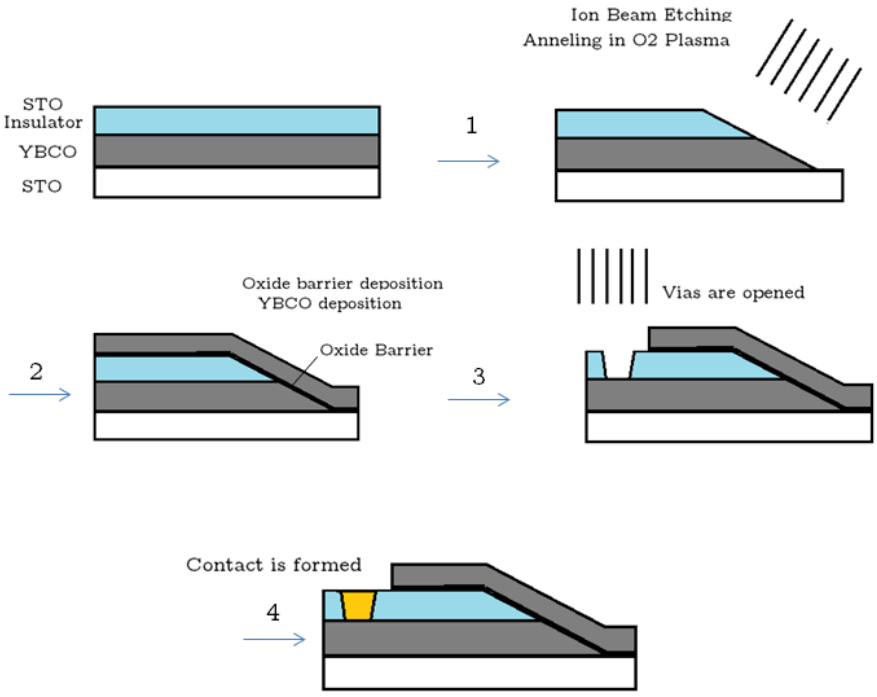


**Figure 3.8:** Fabrication process of SIS-ramp edge weak links

After successfully depositing the superconductor a thick insulating layer is formed. (1) this three layer structure is etched directionally by ion beam etching (IBE) to form a ramp. In order to reduce the damage from the IBE it is annealed in oxygen plasma. (2) To form a barrier an oxide layer is deposited. The barrier thickness is around 5-25 $nm$. Then it is followed by the deposition of the top superconducting electrode. (3) In order to have a contact to lower electrode vias are opened by IBE through the insulating thick layer. (4) the vias are filled with the contact material.

Superconducting electrodes have C-axis orientations. In order to avoid grain boundary formation in the top electrode and have an effective barrier, the angle of ramp is varied between $10^o$ and $20^o$. The advantage of this junction type is that the top electrode shields the magnetic field normal to film surface so that they can perform in unshielded environments. Also barrier interfaces are not in contact with the environment. Key factor in ramp

edge junctions are the barrier quality and thickness. If the damage is not annealed in step (1) the critical current is deterred by an order of 3[18]. The barrier thickness is typically around 5-50 nm depending on the material. However increasing the barrier thickness will reduce the critical current dramatically[13].

### 3.7.3 Intrinsic Junctions

Josephson junctions with intrinsic interfaces are strongly depended on the anisotropy of superconductors. Weak coupling due to ab planes of each superconductor by a grain boundary barrier is a typical example of intrinsic junctions. The grain boundary is formed with different orientation of superconductors are brought together. Typically, the superconductor materials are deposited on bicrystal substrates. The resulting electrodes will have the same angle difference with substrate.First Josephson effects in HTS films are observed naturally occurring in poly-crystalline superconductors. Chaudhari et al. [19] were first to recognize grain boundary junctions on YBCO films to be used as Josephson junctions.

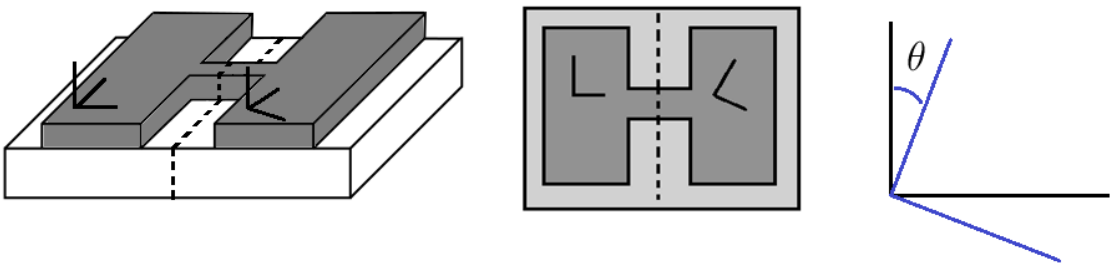


**Figure 3.9:** Schematic representation of grain boundary junctions.

This type of junction fabrication is very straight forward thus making it most reliable and successful junction type currently. Typical bicrystal substrates for junctions are MgO, $LaAlO_3$ and $SrTiO_3$. Currently, there are substrates used having angle values between $10^o$ to $50^o$ but the most used ones have the angle variation of $24^o$ and $30^o$. The behaviour of

the junction and the critical current strongly depends on the angle. If the angle is higher than the critical value of $10^o$, the junction behaves as resistively shunted model, which is to be discussed in the following chapter[20]. Thus the junction will be non-hysteric. However increasing the angle also reduces the critical current. It is reported that critical current will decrease exponentially[4](see figure 3.10).

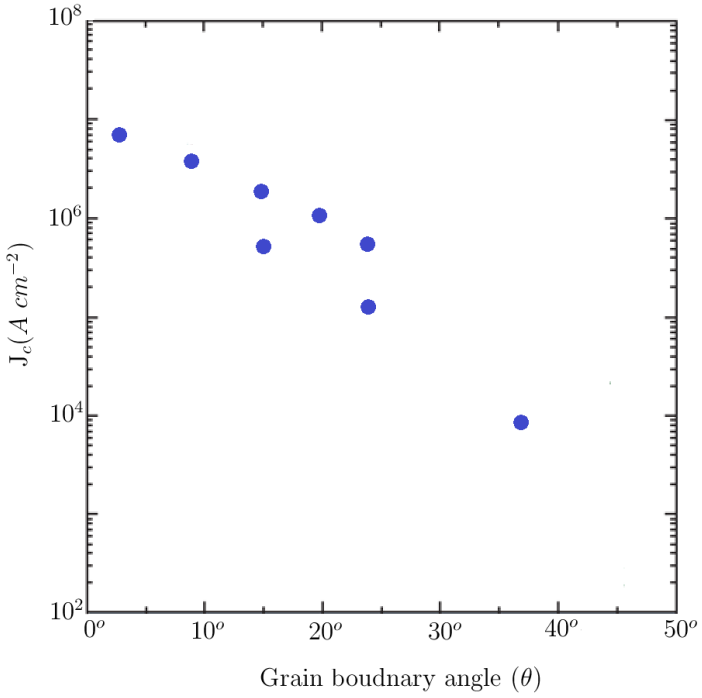


**Figure 3.10:** Graphical representation of angle dependence of critical current density[4].

For a fixed $\theta$, annealing the grain boundary in oxygen atmosphere will affect the thickness of the barrier thus the critical current density can be increased by an order of magnitude[21]. Typical critical current values for GBJ are $10^4\ A/cm^2$. Grain boundary junctions are very stable over long period of times and show high reproducibility, that is, there is nearly 20% tolerance in critical current. However the junctions are limited along the grain boundary.

Bicrystal and ramp edge junctions are more popular and commercially available junc-

tion types. This is due to ramp edge junctions' easy integration to complex circuits, being natural shield for magnetic field, having a large coherence length in ab plane and having good control over critical current[22]. Bicrystal junctions are highly ohmic which is desired in squid applications, and have good control over critical current with boundary angle. They also have large coherence length in ab planes. Since only one single layer of superconductor is needed, fabrication steps for bicrystal junctions are straight forward to develop high quality and highly reproducible devices. Considering these aspects, ramp edge and bicrystal grain boundary junction are more studied and developed devices.

# Chapter 4

# High Temperature DC SQUIDs

Superconducting QUantum Interface Devices (SQUIDs) are currently the most sensitive magnetic flux detectors available[15]. They are able to measure any physical quantity that can be related to magnetic flux. SQUIDs are based on two principal phenomena that are discussed in earlier chapters. First one us the flux quantization in superconducting loop and the other is Josephson tunneling. There are two types of squids when the circuit design is considered. The outputs of these devices, rf and dc SQUIDs, will be periodic with $\Phi_0$ in applied magnetic flux to the loop. In this Chapter, a brief overview of theory and practice of the SQUIDs are discussed

## 4.1 DC SQUID

DC SQUID is composed of a superconducting loop containing two Josephson junctions. For simplicity it is assumed that these junctions are identical and arranged symmetrically. As discussed earlier if the current driven through the junctions $I$ is higher than $I_c$, there will be a voltage drop across the device. Figure 4.1 illustrates a simple SQUID design.

The total current will be the addition of the currents through X and Y. Lets denote the current densities in each junctions as $J_X$ and $J_Y$ with respective phase differences $\phi_X$

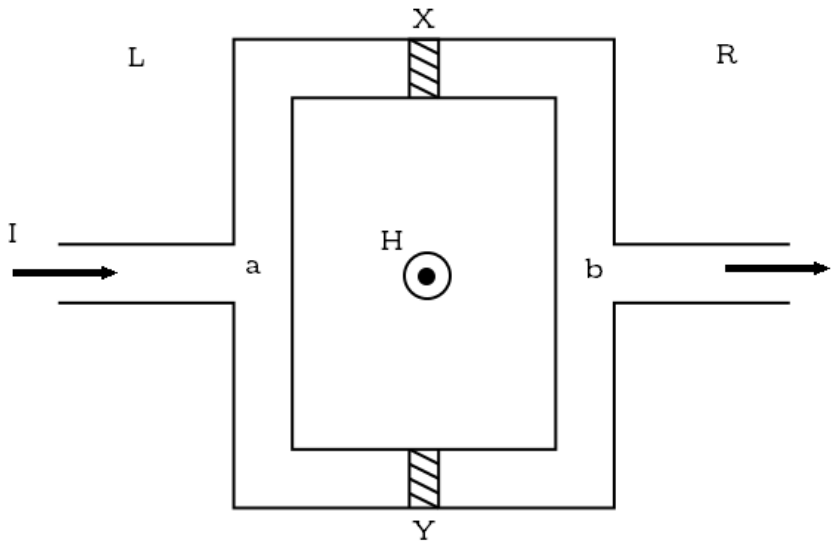


**Figure 4.1:** Schematic representation of DC SQUIDs.

and $\phi_Y$. The phase difference between point a and point b should be independent of the path taken. Thus it is equal if gone through either junctions. Along the path containing junction X, the phase difference between point a,b is given as:

$$\Delta P_{a\to b} = \phi_X + \frac{e^*}{\hbar}\int_{P_X} \vec{A}\cdot\vec{dl} \tag{4.1}$$

Similarly the phase difference through the junction Y is given as:

$$\Delta P_{a\to b} = \phi_Y + \frac{e^*}{\hbar}\int_{P_Y} \vec{A}\cdot\vec{dl} \tag{4.2}$$

These equations must be same. If it is subtracted , these equation will lead to:

$$\phi_Y - \phi_X = \frac{e^*}{\hbar}\int_{loop} \vec{A}\cdot\vec{dl} \tag{4.3}$$

The integral along the loop is the magnetic flux through the loop. The equation 4.3 becomes:

$$\phi_Y - \phi_X = \frac{e^*}{\hbar}\Phi \tag{4.4}$$

Here it is seen that the phase differences are varied with the applied magnetic flux. In order to simplify further the phase differences can be rewritten as:

$$\begin{aligned} \phi_X &= \phi_{arb} + \pi\frac{\Phi}{\Phi_0} \\ \phi_Y &= \phi_{arb} - \pi\frac{\Phi}{\Phi_0} \end{aligned} \tag{4.5}$$

Here $\Phi$ is the applied magnetic flux and $\Phi_0$ is the magnetic flux quantum($\Phi_0 = h/e^*$). Remembering the current density relation of the Josephson junction (equation 3.10) the total current will be expressed as $J_{tot} = J_X + J_Y$:

$$J_{tot} = J_0\left[\sin(\phi_{arb} + \pi\frac{\Phi}{\Phi_0}) + \sin(\phi_{arb} - \pi\frac{\Phi}{\Phi_0})\right] \tag{4.6}$$

Using trigonometric identities equation 4.6 becomes:

$$J = 2J_0\sin(\phi_{arb})\cos(\pi\frac{\Phi}{\Phi_0}) \tag{4.7}$$

For an applied magnetic flux, the Josephson current is maximized by taking $\sin\phi_{arb} = 1$.

$$J_{max} = 2J_0\left|\cos\pi\frac{\Phi}{\Phi_0}\right| \tag{4.8}$$

The tunneling current exponentially depends on the barrier thickness. The applied field covered by these junctions will not be the same if they are not identical. Thus these two junctions are desired to be symmetrical. Figure 4.2 illustrates the maximum total current behaviour of the device with individual critical junction currents over applied magnetic field. The interference pattern is significantly destroyed if the barrier thicknesses are different.

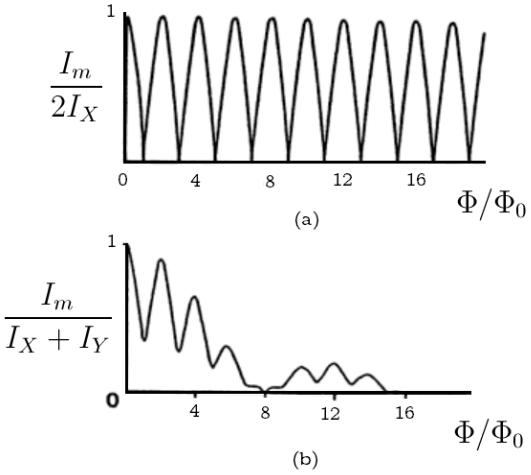


**Figure 4.2:** Normalized critical versus applied flux of a) $I_X = I_Y$. b) $I_X = I_Y/2$ [12].

After the discovery of HTS materials, the possible applications of the high $T_c$ SQUIDs have been realized and extensively studied[10]. The major outcome of the HTS materials is that devices can be constructed such that they can operate in liquid nitrogen temperatures, which is relatively cheap compared to low temperature cooling systems. However, the fabrication of these devices must be well understood and optimized. Thus junctions with high reproducibilities are desired. Figure 4.3 represents the current voltage characteristics of a dc SQUID made from HTS material , YBCO.

When the current is above the critical limit, voltage is modulated by the applied flux. However the applied current will have effect on this modulation. Thus the SQUID is biased to have a larger modulation in voltage in order to achieve better sensitivities. Figure 4.4 illustrates the voltage modulation over applied flux with different biased currents.

It is seen that, the amplitude of oscillations increases to a maximum and decreases as the bias current changes. The SQUID is operated at bias current which gives the maximum corresponding voltage.

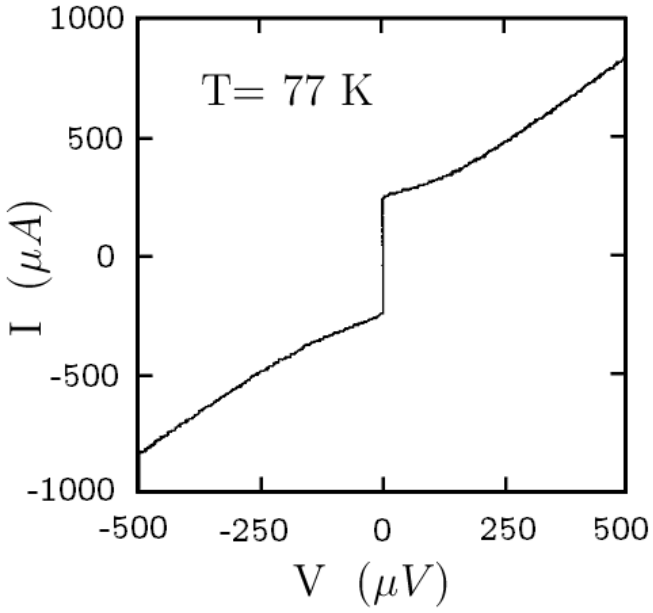


**Figure 4.3:** I-V characteristics of bicrystal dc SQUID at 77 K. Here $I_0 = 120\mu A$ [23].

## 4.2 The Resistively Shunted Junction

It is generally required for SQUIDs that the I-V characteristics are non-hysteric. For hysteric devices, when the current increases from zero, the voltage is developed when current exceeds the critical value $I_0$. However while reducing the current the same effect is not observed. The voltage disappears when the current is much less then the critical value. In practical applications it is needed to be eliminated. The non-hysteric characteristics are obtained when the Josephson elements of the SQUID is resistively shunted. The junction becomes parallel with the resistance and self capacitance. The equation of motion for the junction is given as[15]:

$$C\dot{V} + I_0 \sin\phi + V/R = I + I_N(T) \tag{4.9}$$

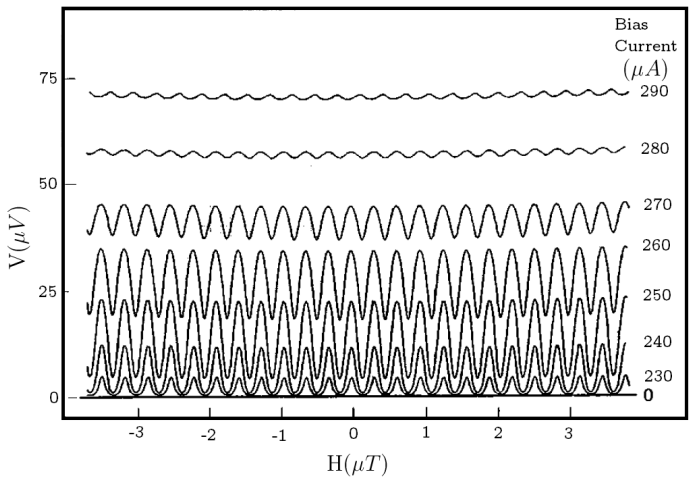


**Figure 4.4:** Voltage modulation over varying flux with different values of applied bias current [23].

Neglect the noise term associated with the noise in current of shunt resistance R. Remembering the Josephson equation $V = \hbar\dot{\phi}/e^*$ the equation 4.9 yields to:

$$\frac{\hbar C}{e^*}\ddot{\phi} + \frac{\hbar}{e^* R}\dot{\phi} = I - I_0 \sin\phi = -\frac{e^*}{\hbar}\frac{\partial U}{\partial \phi} \tag{4.10}$$

where

$$U = -\frac{\Phi_0}{2\pi}(I\phi + I_0 \cos\phi) \tag{4.11}$$

The equation 4.11 is analogous to the potential of the tilted washboard in which a ball is moving. For the current values lower than the critical value, $I_0$, the particle is confined in one of the potential wells represented in figure 4.5 and oscillates in these well with a certain frequency. In this case, time average of $\dot{\phi}$ is zero and this implies that the voltage across the junction is zero. When the current is above $I_0$ than there will be no local potential well, thus the particle will keep moving on the tilted potential. The time average of the $\dot{\phi}$ in this case is not zero. Hence there will be a potential difference developed on the junction. As current increases the voltage across the junction increases as well. For the non-hysteric

case it is required that the voltage drop vanishes as soon as the current is reduced below the critical value, $I_0$.

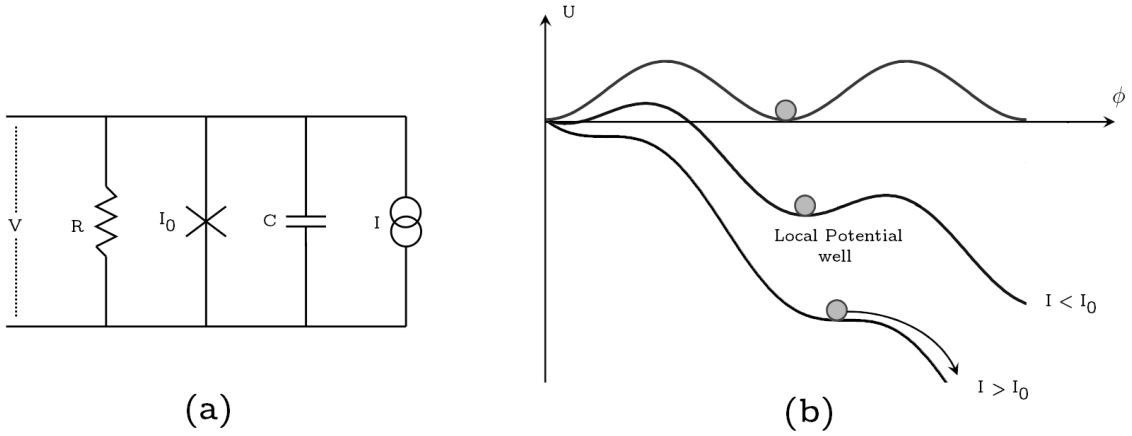


**Figure 4.5:** a) Schematic representation of the resistively capacitevly shunted junction b) Potential energy U versus phase with different applied current. $I < I_0$ represents the trapping of the particle in local potential well.

Lets define a damping parameter $\beta_c$ which was first introduced by Stewart and McCumber.

$$\beta_c \equiv \frac{2\pi I_0 R}{\Phi_0}(RC) = w_j RC \tag{4.12}$$

Lets discuss the state where the $\beta_c << 1$ which is often observed high $T_c$ junctions. The capacitive term in equation 4.10 becomes negligible. If the $B_c$ is neglected the solution for voltage becomes:

$$\begin{aligned} V &= 0 && for \quad I < I_0 \\ V &= I_0 R\left[\left(\frac{I}{I_0}\right)^2 - 1\right]^{-\frac{1}{2}} && for \quad I > I_0 \end{aligned} \tag{4.13}$$

Equation 4.13 describes a non-hysteric behaviour when the current is changed.

There is another parameter that affects the current voltage characteristics. Ideally the squid with low inductance and ideal current will have a critical current modulation between $2I_0$ and 0. Lets define screening parameter as $\beta_L = 2LI_0/\Phi_0$. This term will have an effect on current modulation, that is the lower limit zero is changed. The screening current due to applied field will be proportional to quantized amount of $\Phi_0/L$ which leads to $J_{sc}/I_0 = 1/\beta_L$. Hence the minimum critical current will be $2(I_0 - J_{sc})$.

## 4.3 Sensitivity

Practical SQUIDs not only have ability show non hysteric characteristics for magnetic field and current also they are limited by the noises which are due to thermal fluctuations, fluctuations in critical current and vortex motion. In order for a SQUID to operate at maximum sensitivities, the $\beta_c$ and $\beta_L$ parameters should be smaller than unity, 1. The

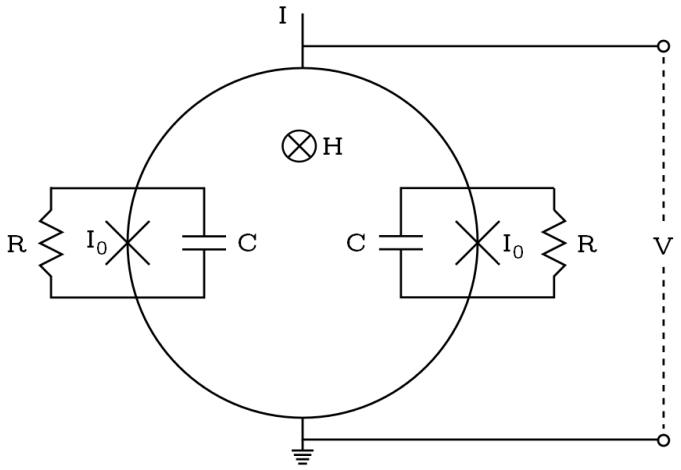


**Figure 4.6:** Schematic representation of resistively shunted DC SQUIDs.

energy of thermal fluctuations should not be greater than the coupling energy between superconductors in a junction which corresponds to be around $5k_BT$. Any thermally

generated currents in the loop will generate a flux thus there will be a noise magnetic flux through the loop. This effect is strongly depended on the self inductance of the loop. Thus lowering the capacitance and inductance of the loop will yield to better sensitivities. This case can be achieved by building SQUIDs with smaller dimensions. A similar calculation is done by Ketchen et al[24]. They introduced a parameter known as spin sensitivity. The found the equation for spin sensitivity as:

$$S_n = \frac{a\phi_{n1}}{2\pi\mu_B} \tag{4.14}$$

where $a$ is the radius of the squid loop and $\mu_B = 9.27 \times 10^{-}24J/T$ is the Bohr magneton. They defined the flux noise $\phi_{n1}$ as:

$$\phi_{n1} \propto TL^{3/4}C^{1/4} \tag{4.15}$$

Reducing the dimensions of the squid will lead to smaller inductance and if all dimensions are scaled uniformly than the capacitance is also reduced. But smaller loop area will contradict to flux however it is expected that the overall sensitivity is increased.

## 4.4 DC SQUID Configuration

In this section two main type of SQUID configurations are investigated. Figure 4.7 illustrates the schematic representation of these two type configurations. First one is hole like configuration and it is more suited for flux flow transistor. Although it is not suitable for magnetometer applications strong signals can be obtained. That is because the inductance component from narrow lines are eliminated. It is also used to study the principles of a junction or device. The second configuration is more suited for magnotemeter applications because the junctions are out of the effective magnetic field flux area[25]. In this work a hole like configuration is used.

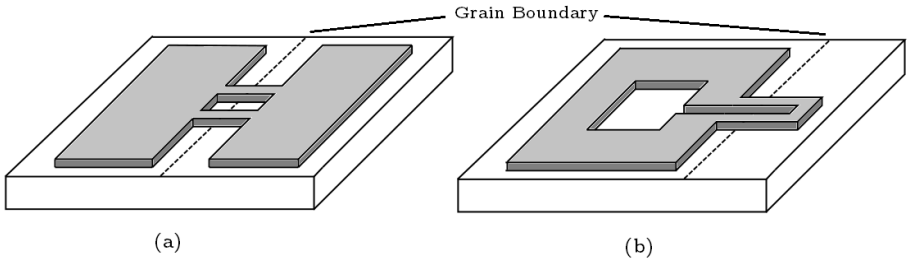


**Figure 4.7:** a) A hole like geometry, b) A washer like geometry for SQUID configurations.

# Chapter 5

# Experimentation

In this chapter the detailed steps of growth of YBCO thin films and fabrication of DC SQUIDs are investigated. After the discovery of the high temperature superconductors many other materials are investigated and discovered to be superconductor above the temperature 77 K. Among these, $Y_1Ba_2Cu_3O_7$ is the most studied thin film structure. The transition temperature is around 90K and critical current densities in good quality films are found to be $10^6 A/cm^2$. Lattice parameters are $a = 3.82$ Å, $b = 3.89$ Å and $c = 11.68$ Å. With the anisotropy in YBCO films, bicrystal Josephson junctions are realized and extensively used. In our work, dc SQUIDs are fabricated on bicrystal substrates. YBCO films are sputtered and and patterned with e-beam lithography and dry etching. In following sections, fabrication methods are discussed and respective results are given.

## 5.1 Thin Film Deposition

There are several methods to grow thin films such as e-beam evaporation, pulsed laser deposition and sputtering systems. In our work an RF magnetron sputtering system is used which is a kind of physical vapour deposition. RF magnetron sputtering has a vacuum chamber that consist of sputtering target and substrate holder. The system that we used

has two gas inlets to create a plasma. There are different types of configurations of the substrate holder and target used on YBCO growth, on-axis[26] and Off-axis[27].

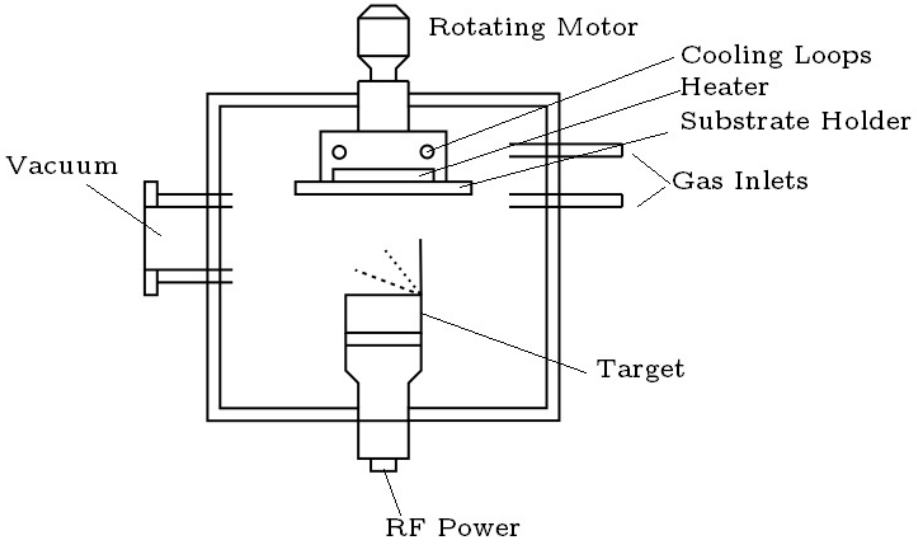


**Figure 5.1:** Schematic representation of RF magnetron sputtering.

The plasma is created with the applied power, which ionizes the inlet gas. The electron removed from the gas is then rejoined to sustain plasma. The ions will the accelerate towards to target and strike. There are several outcomes of the collision. First one is that the atoms of the target material is removed and deposited on the substrate. Second one is, there are secondary electron produced due to collision and scattered back in the chamber. This electron can be used to sustain plasma as well. Third one is that, the bombarding gas ions are reflected back, so there is a high possibility that these ions will hit substrate and lead to back sputtering. The RF magnetron system is designed such that there are permanent magnets under the target, creating a local trapping magnetic field for charged particles. This situation will lead to more confined and denser plasma since the electrons and ions circulate around the magnetic field. This will result in increased deposition rates. Due to collision, there may be some positive charges accumulated on the target surface.

If the these charges are not neutralized the electric field my be ceased thus destroying the plasma. Thus an RF power is used to alternate the electric field. Another important aspect is that, to reduce back sputtering the substrate-target configuration is changed from on-axis($0^o$) to off-axis($90^o$). To summarize in order to have a good deposition rates with minimal damage to substrate region is to use off-axis configuration and to use magnetron system.

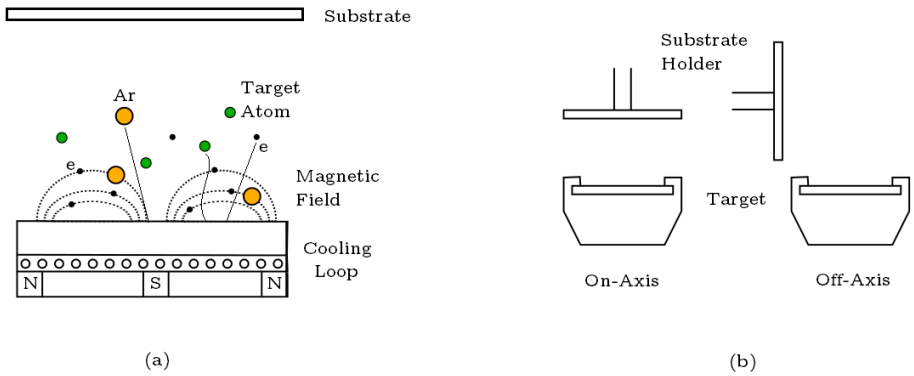


**Figure 5.2:** a) A sketch showing possible outcomes of collision between Argon ions and target. Magnetic field is created by permanent magnets under target material. b) Two target-substrate configurations.

In order to have a high crystalline thin films, it is needed that the lattice match is observed. Thus using proper substrates with certain temperatures will lead to good quality films of YBCO. Generally $SrTiO_3$, $LaAlO_3$ and MgO are used as substrates for YBCO thin films. Among these, bicrystal(24 degree) (100) STO ($SrTiO_3$) is used in our experiments. STO has a simple cubic structure having a lattice parameter of 3.9 Å. For STO it is reported that optimum temperature is around 720 $^0C$[28]. In our experiment,(a) with on-axis configuration, substrates are placed 15mm above (target center) and parallel to target and heated to 720 $^0C$.(b) Also off axis configuration are used with 2.5 cm height without heating. To obtain more uniform films, substrates are rotated. Target materials have a circular area having a radius of 2 inches and substrates have a dimensions of 5x5x1 mm.

Substrates are cleaned with acetone and isopropanol alcohol in ultrasonic bath before

deposition. In some cases it is carried out that substrates are treated with argon plasma. The system is vacuumed to a base pressure of $1.2 \times 10^{-5} mbar$ . Then the pressure is set to 100 mTorr with an argon to oxygen ratio of 4:1. The RF power is set to 70 $W$. The deposition rate for setup (a) is found to be zero. This is due to relatively long distance between the substrate holder and target. The on axis configuration (b) led to a rate of 10nm/min.

## 5.2 Annealing and Oxidation

Although it is preferred to heat the substrate during deposition, there are several studies show post annealing of YBCO films[29]. Thin films grown with off-axis non heating configuration are annealed. The annealing process carried out in 29 $Pa$ pressure and at 750 $^oC$. The duration for this process is 0.5 hour to 3 hours. It is also required that the pressure is lowered from 0.3 $mbar$ to 0.003 $mbar$ Temperature increase is rapid however cool down is adjusted at a rate of 6 $C^o/min$. In order to prevent the possible oxygen loss then these films are subjected to oxidation process. It is carried out in 300 Torr oxygen atmosphere at 500 $^oC$. The oxidation duration is 1 hour. After oxidation the temperature is lowered to room temperatures with same rate. The stability line must be followed in order to have superconducting properties. The stability lines are given in figure 5.3, which reports the successful growth of YBCO films[30].

## 5.3 Contact Deposition

In order to have a non hysteric characteristics of the junctions, YBCO thin films needed to be shunted. For this purpose, deposition of gold on YBCO films are generally preferred. Another useful aspect of using gold as shunt resistor is that it can be used also for making contacts to YBCO films which will result in more ohmic contacts. It is generally required

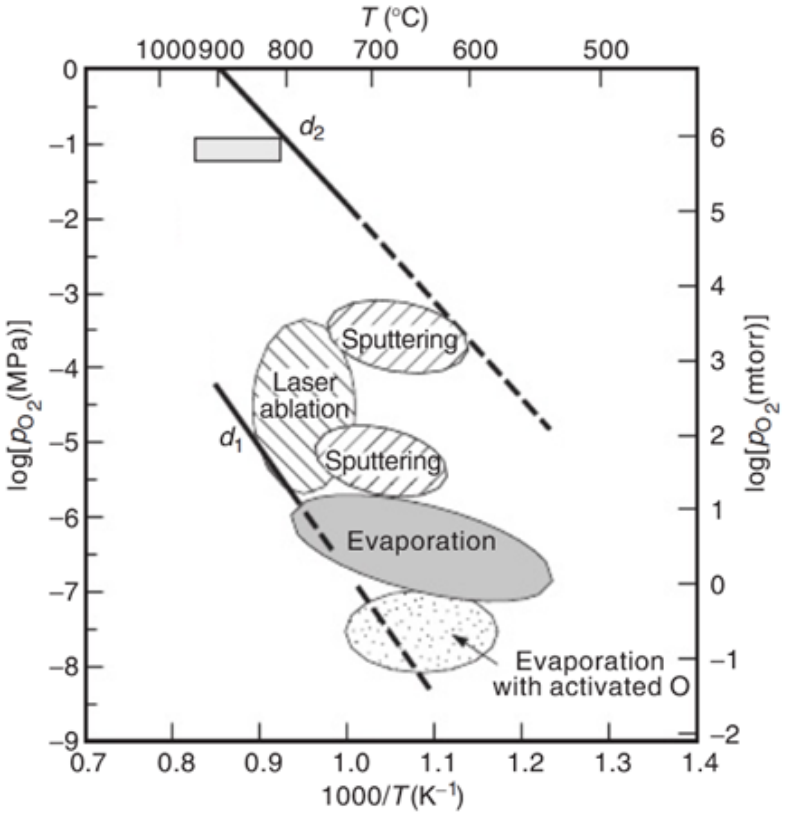


**Figure 5.3:** Oxygen stability lines for YBCO[30].

that in order to have uniform and better contacts, Au should be deposited in-situ. However ex-situ deposition of contact metals are reported[31]. Ex-situ gold are deposited on YBCO films using DC-Sputtering systems using argon gas. The rate for the deposition is 2.5 $nm/min.$ a 50nm thick contact layer is deposited on YBCO films.

## 5.4 $SiO_2$ Deposition

After the contact deposition, a $SiO_2$ layer is deposited to act as a hard mask for dry etching process. This layer is deposited with RF magnetron sputtering system. The plasma gas is argon and the respective pressure is set to 3 $mTorr$. The on-axis configuration is used with a target-substrate distance of 15 $cm$. The respective RF power for this deposition process is 150 $W$. The resulting rate is 40 $nm/h$.

## 5.5 Lithography

Our work is to fabricate junctions on narrow YBCO loop bridges having dimensions of 200 $nm$. This resolution is easily achieved by electron beam lithography. After the deposition of the masking layer, an e-beam resist is coated on the surface. For this purpose a negative resist is used. Since the junctions are formed on grain boundary it is a faster process if negative resists are used. That is, the electron illuminated regions in negative resist will not decompose in the respective developer solution. In this work polystyrene having a molecular weight of 170 $kg/mol$ is used as negative resist. Spin coating of PS with a 2000 rpm results in around 100 nm of thickness. To pattern PS, 5 $kV$ of electron beam voltage is used. The dose is found to be as 20 $\mu C/cm^2$.

## 5.6 Etching Process

Wet etching of the YBCO is rather omitted because certain water soluble solution will degrade the superconductivity due to the oxygen loss during the process. Thus alternative etching methods are investigated. Reactive ion etching[32] and sputter etching system are realized. In our work YBCO is etched in sputtering system using the substrate cleaning function which creates a plasma around the substrate. The power is 50 $W$ and the pressure is around 100 $mTorr$. In order to determine the etch rates half of the film is covered with

thick resist and then subjected to etch process. Then the resist is removed and the difference in thickness is analyzed with the help of atomic force microscopy. The etch rate for YBCO is found to be around 1.5 $nm/min$.

Etching of the $SiO_2$ is realized in two systems. One is reactive ion etching. The etchant gases are $CF_4$ and $O_2$ with a pressure ratio of 10:1 in a total pressure of $20mTorr$. With 100 $W$ applied RF power the etch rate is found to be 120 $nm/min$. This method of etching is used to transfer the pattern from e-beam resist to $SiO_2$ layer. The other method is the physical dry etching using sputtering system. This can be used to remove the $SiO_2$ layer properly during the etch process of YBCO and Au. The rate is found to be as 1.4 $nm/min$.

| Material | Rate(RIE) | Rate(Sputter) |
|---|---|---|
| YBCO | | 1.5 nm/min |
| Polystyrene(PS) | | 40 nm/min |
| PMMA | | 75 nm/min |
| $SiO_2$ | 120 nm/min | 1.4 nm/min |
| Au | | 10 nm/min |

**Table 5.1:** Measured etch rates for different materials used during fabrication steps.

## 5.7 Fabrication Steps

The fabrication steps for building a dc SQUID is rather straight forward. These steps are represented in figure 5.4.

1. After proper cleaning of bicrystal substrates, 100 nm thick YBCO is deposited with RF magnetron sputtering. DC sputtering of 50 nm Au is then followed. Another RF magnetron sputtering is done to obtain 100 nm $SiO_2$. Finally the resist is spin coated on $SiO_2$ for about 100 nm.

2. The resist is patterned with electron beam lithography (EBL) and developed in tetrahydrofuran (THF). The dimensions of the device is shown in figure 5.5.

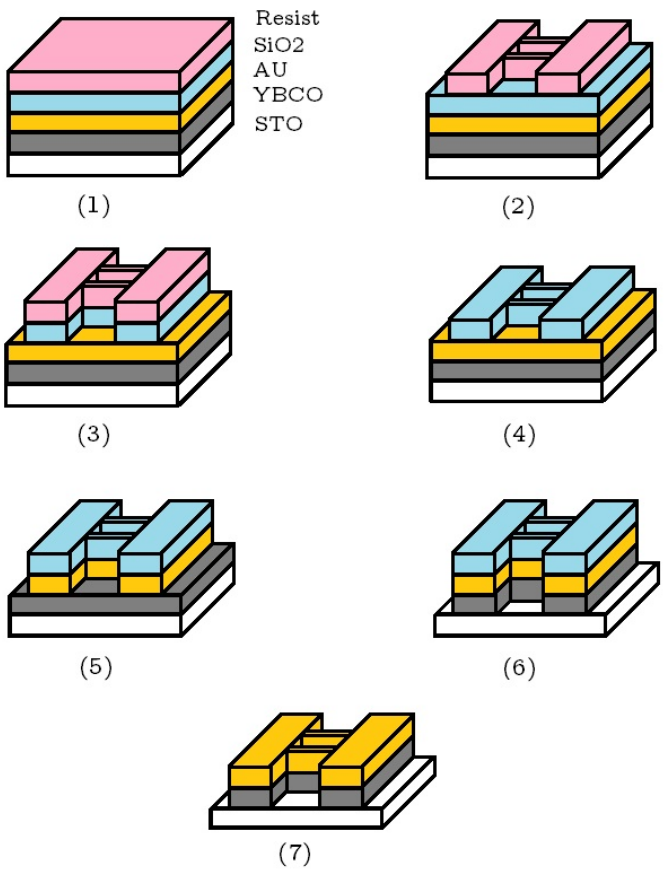


**Figure 5.4:** Schematic representation of fabrication steps.

3. The pattern is then transferred to $SiO_2$ with RIE.

4. The e-beam resist is then removed for further etching.

5. Gold is then etched with sputtering system to follow the pattern.

6. The pattern is then transferred to YBCO with sputter etching. During the etch process $SiO_2$ is used as hard mask for argon plasma etching.

7. Then the $SiO_2$ layer is removed either RIE or sputter etching.

If the thicknesses and etching rates are calculated correctly the carefully deposited $SiO_2$ layer will be both used as hard mask and removed in a simple etching step through (4) to (7).

## 5.8 Characterization

After the deposition of thin films, structural characterizations are then performed. For this purpose, Scanning Electron Microscopy(SEM) , Energy Dispersive X-ray spectroscopy(EDX) and Back Scattering Imaging are used. To analyze the surface Atomic Force Microscopy (AFM) is used. As well as being used for electron beam lithography, SEM is capable of giving strong insight about the devices on surface of the structures and relative information about the phases of the sample. With the help of back scattering detector, phases consisting the films can be analyzed. Different phases have different colours in the resulting image.

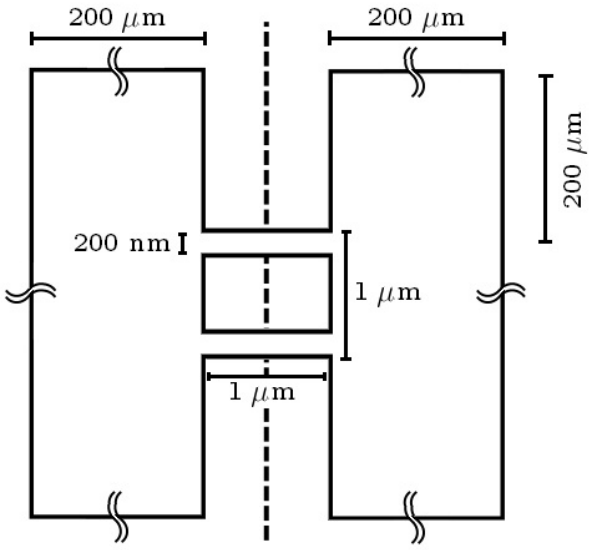


**Figure 5.5:** Schematic representation of hole like geometry DC SQUID.

EDX is used to determine the concentration of individual atoms. It relies on the idea that the energetic photons will excite electron is each atoms in scanned region. This excited electron will then relax and emit a photon with respective energy. The energy scale is well defined and concentration of the structure is then realized. AFM is used to determine the height differences on the surface.

The electrical and magnetic characterizations are carried out at Brockhouse Institute of McMaster University. Magnetic characterizations are done by a magnetic properties measurement systems (MPMS) with SQUIDs. First step is to observe a diamagnetic transition. Second is the electrical characterization over varying temperatures.

## 5.9 Results and Discussions

During the film growth process there are many factors that affect the overall quality of the film. However it is tried to be optimized. One of the factors is that the distance between target and substrate should be in logical limit to observe uniform films. On-axis configuration 15 cm distance led to no film growth and off-axis configuration resulted in 10nm/min rate of deposition. However this rate seems to be a little high to let good nucleation during deposition. Figure 5.6 shows the a) SEM image of the films without heating and oxidation and b) SEM image of the post-annealed oxidized samples .

It is clearly seen the the annealing process led to more segmentations on the surface. With the proper EDX analyses on the background film and these segmentation will lead us to suspect that these segmentations copper-oxides. The results are shown in table 5.2. The copper element tends to desorb second after oxygen thus it is more favorable to form copper-oxide crystals during post-annealing. This copper-oxide domination may be corrected by using more suitable temperatures and increasing the oxygen pressure during oxidation. Back scattering image also shows the difference in between these two regions, see figure 5.7

The non-uniformity of the surface will lead to devices with rough surfaces as well. The

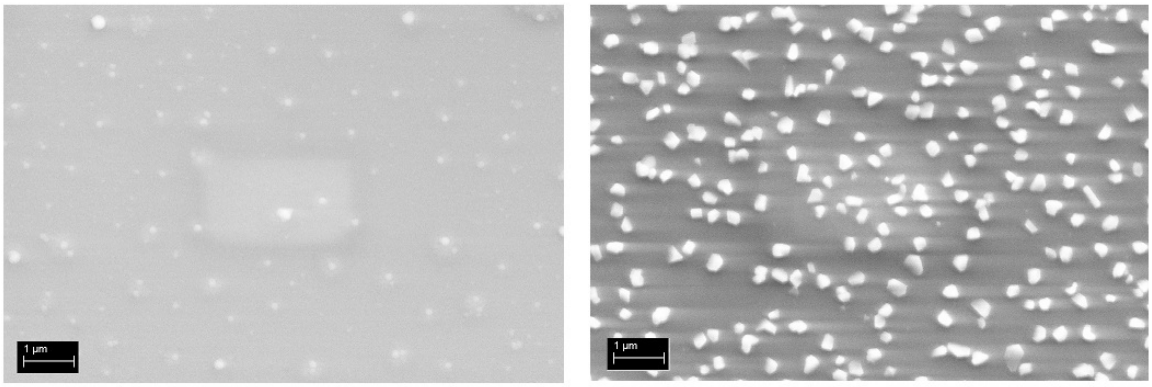


**Figure 5.6:** a) SEM image of YBCO films deposited without heat and no post treatment made. b) After 1 hour annealing and 3h oxidation, more segmentation occurred on films. The scale is $1\mu m$.

| Elements | Background (%) | Segmentation (%) |
|---|---|---|
| Y | 7.99 | 6.37 |
| Ba | 19.26 | 14.97 |
| Cu | 22.76 | 27.87 |
| O | 48.99 | 49.78 |

**Table 5.2:** EDX result on film (b) with different spots as background and segmented regions.

non uniformity is transferred to both gold and silicon dioxie thus anneling may result in devices with smooth surfaces. It is believed that 100 nm thickness of YBCO is enough to carry superconductivity after patterning.

In EDX measurements, oxygen responds to small energies thus it is highly probable that the concentration of the oxygen is not exact. Besides the substrates STO includes oxygen also. With the films having thicknesses of 100nm , the result may include substrate materials as well.

STO substrates are purchased as bicrystal and having an orientation difference of $24^o$. Both regions are c-axis oriented. The grain boundary is visible under SEM after the plasma cleaning. The defects are aligned on the boundary and transferred to upper layers.

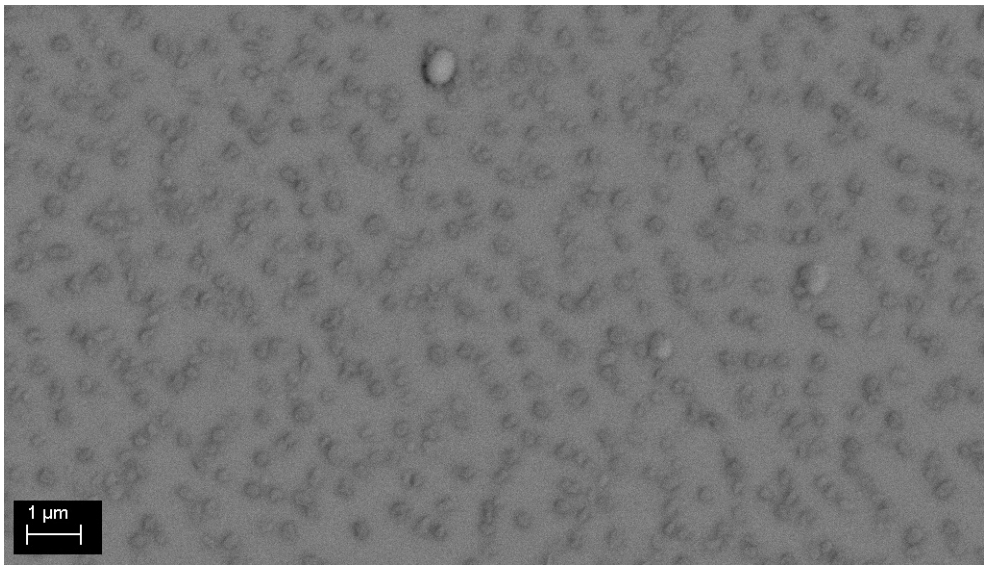


**Figure 5.7:** Back scattering image of annealed films. Scale is $1\mu m$.

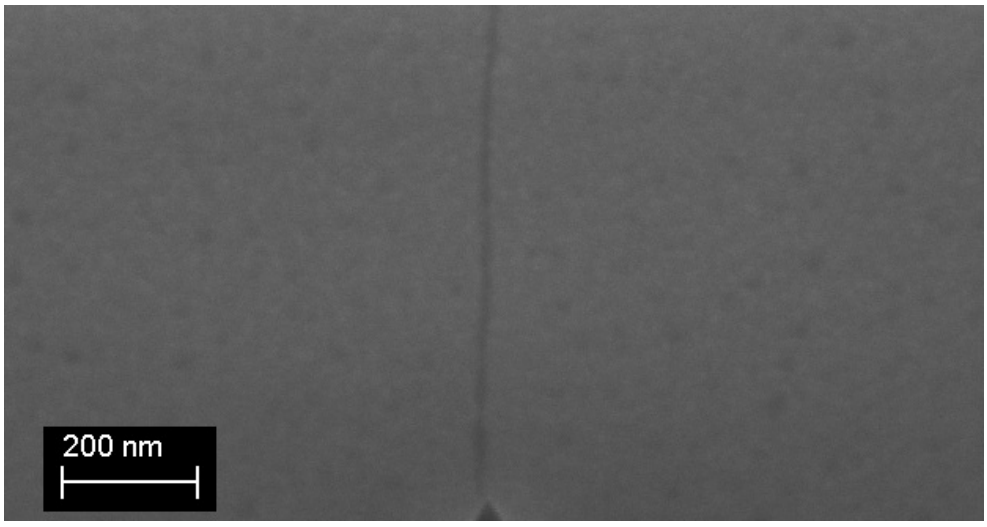


**Figure 5.8:** Grain boundary of STO bicrsytal substrates.

This defected line will help to align the sample for lithography on boundary. Figure 5.8 shows the grain boundary on STO substrate and figure 5.9 shows the defects along the grain boundary on YBCO/Au/$SiO_2$/Ps layer.

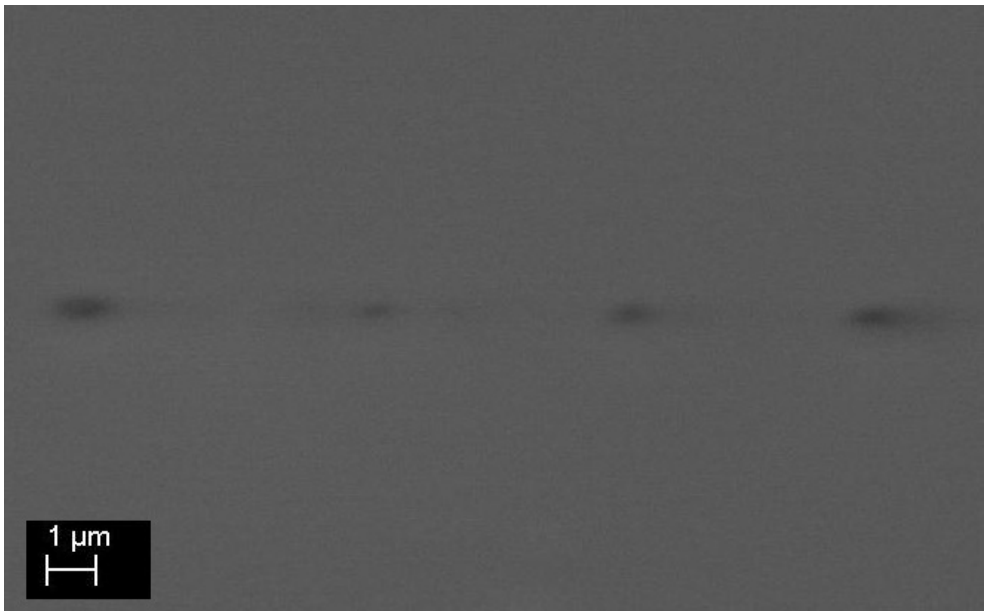


**Figure 5.9:** Defects along grain boundary on YBCO-Au-$SiO_2$-PS.

The magnetic characterization of the YBCO is done at McMaster University. Ac susceptibility measurement showed that films fabricated with RF magnetron sputtering with the paramters mentioned above are not found to be superconducting. The temperture scan is from room temperature to 20 K. However films deposited with pulsed laser deposition show the specific change in the magnetic properties at 89 K. The SEM image of these films are shown in figure 5.10. Respective EDX measurement is shown in figure 5.11.

The EDX result suggests that the conentraion of $Y$ is 7.62 % and the concentration of $Ba$ is 18.16 % and $Cu$ concentration is 22.11 %. It can be said that the correct stichiometry is acquired.

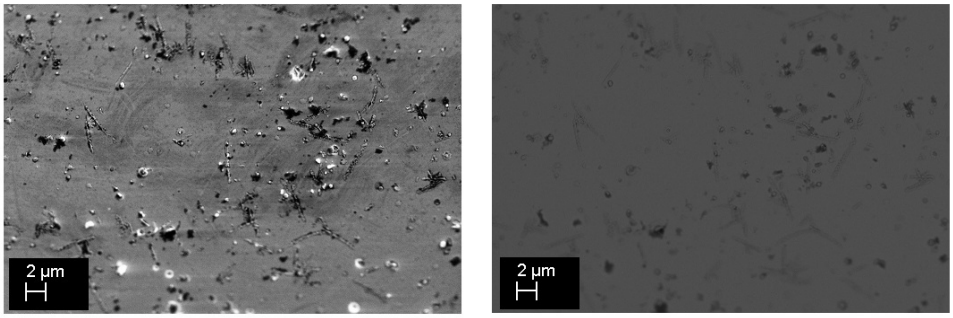


(a) (b)

**Figure 5.10:** a) SEM image of YBCO films deposited with pulsed laser deposition. b) Back scattering image suggests sample is single phase domintaed.

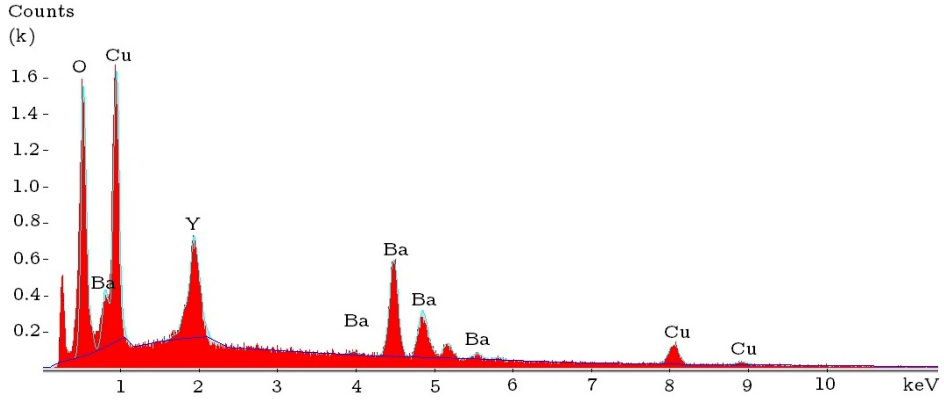


**Figure 5.11:** EDX image of YBCO films deposited with pulsed laser. The graph is obtained by the counting the respective emitted photons from individual atoms versus illumination energy.

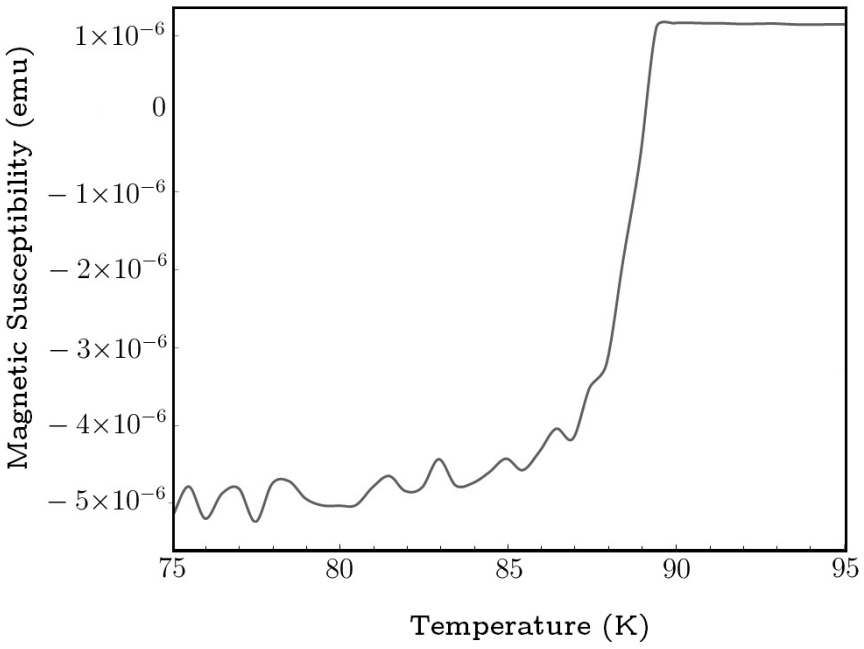


**Figure 5.12:** Magnetic susceptibility versus temperature measurement in 10 Oe. It is clearly showing that the transition occurs at 89 K.

Figure 5.12 show the magnetic susceptibility of the YBCO films. Below the transition temperature YBCO films become diamagnet and repel the applied magnetic field. The transition temperature is 89 K.

# Chapter 6

# Conclusions and Future Work

The fabrication of YBCO films and DC SQUIDs are tried to be realized in this study. YBCO thin films are deposited on STO bicrystal substrates by RF magnetron sputtering. A gold layer iswas deposited on top of YBCO films by DC sputtering to act as both shunting resistor and ohmic contact formation. As hard mask, $SiO_2$ layer was deposited on Au with RF magnetron sputtering. Certain geometry was patterned on the negative e-beam resist PS. After the electron beam lithography, the pattern on the resist was then transferred to silicon dioxide. Then sputter etching of Au and YBCO was carried out. Final device is obtained by removing the oxide layer resulting a shunted YBCO SQUID.

The purpose of this study was to fabricate a nano-scale superconducting quantum devices however, the sputtered YBCO films were not found to be superconducting at temperatures above 20 K. This is rather due to the complex deposition and patterning procedures of the high temperature superconductors. For YBCO, the oxygen content is the main parameter degrading the superconductivity. The oxygen loss can be caused by improper temperatures during growth, annealing and oxidation. E-beam current can also decompose the oxygen from the material. During the etch process, due to argon strike temperature is increased. If the sample is not cooled, superconducting properties will cease. In our setup, the major drawback is the non-adjustable target-substrate dimensions

with proper heating systems. Ideal parameter must be investigated such as distance, temperature, deposition pressure, oxygen stability pressure and proper substrate.

Deposition of gold and oxide layers were straight forward and have been successfully deposited. 200 nm feature size can be easily obtained in electron beam lithography. For the etching process, rates were measured with AFM for YBCO, Au and $SiO_2$ to be as 1.5 nm/min 10 nm/min and 1.4 nm/min respectively in sputter etching process.

In order to characterize, SEM, EDX and magnetic susceptibility measurements were done. These result are not in the expected value range for sputtered film but films deposited with pulsed laser deposition (PLD) systems showed good results. Thus, YBCO can be deposited on bicrystal substrates with PLD.

Regarding the future studies, it can be expected that YBCO film deposited with PLD systems are to be used. In order to increase the sensitivity the scale of the SQUIDs may be reduced to a level as near the minimum feature size of the scanning electron microscopy as the other fabrication parameters allow to do so. After realizing the ideal Josephson junction on bicrystal grain boundaries, samples can be used in different areas such as quantum information and photon detectors.

# References


[1] H.K. Onnes. The superconductivity of mercury. *Comm. Phys. Lab. Univ. Leiden*, 122:124, 1911.

[2] C. Kittel. *Introduction to Solid State Physics*. Wiley, Hoboken, NJ, 2005.

[3] M. Tinkham. *Introduction to Superconductivity*. McGraw-Hill, New York, 1996.

[4] D. Larbalestier, A. Gurevich, D.M. Feldmann, and A. Polyanskii. High-tc superconducting materials for electric power applications. *Nature*, 414:368–377, 2001.

[5] T. Kobayashi. *Vortex Electronis [ I. E. Electronics] and Squids*. Springer, Berlin, 2003.

[6] AA Abrikosov. Nobel lecture: Type-ii superconductors and the vortex lattice. *Reviews of Modern Physics*, 76(3):975–979, 2004.

[7] J. Bardeen and MJ Stephen. Theory of the motion of vortices in superconductors. *Phys. Rev*, 140(4A):1197–1207, 1965.

[8] T. Orlando. *Foundations of Applied Superconductivity*. Addison-Wesley, Boston, 1991.

[9] RL Fagaly. Superconducting quantum interference device instruments and applications. *Review of Scientific Instruments*, 77:101101, 2006.

[10] Y. Bruynseraede, C. Vlekken, C. Van Haesendonck, and VV Moshchalkov. Fundamentals of giaever and josephson tunneling. *The New Superconducting Electronics*, (251), 1993.

[11] J. Nagel, KB Konovalenko, M. Kemmler, M. Turad, R. Werner, E. Kleisz, S. Menzel, R. Klingeler, B. Büchner, R. Kleiner, and Koelle D. Resistively shunted yba2cu3o7 grain boundary junctions and low-noise squids patterned by a focused ion beam down to 80 nm linewidth. *Superconductor Science and Technology*, 24:015015, 2011.

[12] A. Barone and G. Paterno. The josephson effect. *Physics and Applications*, 1984.

[13] AI Braginski, H. Weinstock, and RW Ralston. Thin film structures. *NATO ASI Series E Applied Sciences*, 251:89–89, 1993.

[14] R.W. Simon, JB Bulman, JF Burch, SB Coons, KP Daly, WD Dozier, R. Hu, AE Lee, JA Luine, CE Platt, et al. Engineered hts microbridges. *Magnetics, IEEE Transactions on*, 27(2):3209–3214, 1991.

[15] J. Clarke. Squids: theory and practice. *NATO ASI Series E Applied Sciences*, 251:123–123, 1993.

[16] C. Francke, A. Krämer, M. Offner, R. Strade, L. Mex, and J. Müller. Ion-beam etching of substrate steps: Sns compared to step-edge grain boundary josephson-junctions. *Applied Superconductivity*, 6(10-12):735–739, 1999.

[17] RH Ono, LR Vale, KR Kimminau, JA Beall, MW Cromar, CD Reintsema, TE Harvey, PA Rosenthal, and DA Rudman. High-tc sns junctions for multilevel integrated circuits. *Applied Superconductivity, IEEE Transactions on*, 3(1):2389–2392, 1993.

[18] Y. Soutome, R. Hanson, T. Fukazama, K. Saitoh, A. Tsukamoto, Y. Tarutani, and K. Takagi. Investigation of ramp-type josephson junctions with surface-modified barriers. *Applied Superconductivity, IEEE Transactions on*, 11(1):163–166, 2001.

[19] P. Chaudhari, J. Mannhart, D. Dimos, C. C. Tsuei, J. Chi, M. M. Oprysko, and M. Scheuermann. Direct measurement of the superconducting properties of single grain boundaries in $y_1ba_2cu_3o_{7-\delta}$. *Phys. Rev. Lett.*, 60:1653–1656, 1988.

[20] R. Gross, P. Chaudhari, M. Kawasaki, and A. Gupta. Superconducting transport characteristics of yba2cu3o7-$\delta$ grain boundary junctions. *Magnetics, IEEE Transactions on*, 27(2):3227–3230, 1991.

[21] M. Kawasaki, P. Chaudhari, and A. Gupta. $1/f$ noise in $y_1ba_2cu_3o_{7-\delta}$. *Phys. Rev. Lett.*, 68, 1992.

[22] MI Faley, U. Poppe, K. Urban, E. Zimmermann, W. Glaas, H. Halling, M. Bick, H.J. Krause, DN Paulson, T. Starr, et al. Operation of hts dc-squid sensors in high magnetic fields. *Applied Superconductivity, IEEE Transactions on*, 9(2):3386–3391, 1999.

[23] D. Koelle, R. Kleiner, F. Ludwig, E. Dantsker, and J. Clarke. High-transition-temperature superconducting quantum interference devices. *Reviews of Modern Physics*, 71(3):631, 1999.

[24] MB Ketchen, DD Awschalom, WJ Gallagher, AW Kleinsasser, RL Sandstrom, JR Rozen, and B. Bumble. Design, fabrication, and performance of integrated miniature squid susceptometers. *Magnetics, IEEE Transactions on*, 25(2):1212–1215, 1989.

[25] E. Sarnelli, G. Testa, C. Camerlingo, B. Ruggiero, and M. Russo. Sputtered ybco bicrystal dc-squids. *Journal of Superconductivity*, 9(5):513–517, 1996.

[26] AM Kadin, PH Ballentine, J. Argana, and RC Rath. High temperature superconducting films by rf magnetron sputtering. *Magnetics, IEEE Transactions on*, 25(2):2437–2440, 1989.

[27] CB Eom, JZ Sun, BM Lairson, SK Streiffer, AF Marshall, K. Yamamoto, SM Anlage, JC Bravman, TH Geballe, SS Laderman, et al. Synthesis and properties of yba2cu3o7

thin films grown in situ by 90 off-axis single magnetron sputtering. *Physica C: Superconductivity*, 171(3-4):354–383, 1990.

[28] LM Wang, HW Yu, HC Yang, and HE Horng. Optimum sputtering conditions on the in-situ growth of superconducting yba2cu3oy films with an off-axis rf sputtering configuration. *Physica C: Superconductivity*, 256(1-2):57–63, 1996.

[29] A. Mogro-Campero and LG Turner. Lower temperature post-annealing of thin films of yba2cu3o7 at lower oxygen partial pressure. *Applied Physics Letters*, 58(4):417–418, 1991.

[30] K. Char and V. Matijasevic. *HTS Film Growth*. John Wiley & Sons, Inc., 2005.

[31] JW Ekin, SE Russek, CC Clickner, and B. Jeanneret. In situ noble metal yba2cu3o7 thin-film contacts. *Applied Physics Letters*, 62(4):369–371, 1993.

[32] YH Im, H.G. Kang, B.S. Han, and YB Hahn. High density plasma etching of y-ba-cu-o superconductors. *Electrochemical and Solid-State Letters*, 4:C77, 2001.